

Application of the Teaching Learning Optimization Algorithm to an Analytical Model of Thunderstorm Outflows to Analyze the Variability of the Downburst Kinematic and Geometric Parameters

~~Analysis of the phase space of the downburst that occurred on 25 June 2021 in Sânnicolau Mare (Romania)~~

Andi Xhelaj¹, Massimiliano Burlando¹

¹ *Department of Civil, Chemical and Environmental Engineering
Polytechnic School, University of Genoa, Via Montallegro 1, 16145 Genoa, Italy*

Correspondence to: Andi Xhelaj (andi.xhelaj@edu.unige.it)

Abstract. Downburst winds, characterized by strong, localized downdrafts and subsequent horizontal straight-line winds, presents significant risk to civil structures. The transient nature and limited spatial extent present measurement challenges, necessitating analytical models for accurate understanding and predicting their action on structures. This study analyzes the Sânnicolau Mare downburst event in Romania, from June 25, 2021, using a bi-dimensional analytical model coupled with the Teaching Learning Optimization Algorithm (TLBO). The intent is to understand the distinct solutions generated by the optimization algorithm and assess their physical validity. Supporting this examination is a damage survey and wind speed data recorded during the downburst event. Employed techniques include agglomerative hierarchical clustering with the K-means algorithm (AHK-MC) and principal component analysis (PCA) to categorize and interpret the solutions. Three main clusters emerge, each displaying different storm characteristics. Comparing the simulated maximum velocity with hail damage trajectories indicates that the optimal solution offers the best overlap, affirming its effectiveness in reconstructing downburst wind fields. However, these findings are specific to the Sânnicolau Mare event, underlining the need for a similar examination of multiple downburst events for broader validity.

KEYWORDS: Downburst analytical model, Metaheuristic optimization algorithm, Multivariate data analysis, Downburst kinematic and geometric parameters, Damage survey.

1 Introduction

The wind climatology of Europe and several mid-latitude countries are primarily dominated by the presence of extra-tropical cyclones and thunderstorms. The understanding of the formation and evolution of extra-tropical cyclones dates back to the 1920s (Bjerknes and Solberg, 1922). The atmospheric boundary layer (ABL) winds generated during such systems are well recognized, and their influence on structures has been extensively studied and coded starting from the 1960s (Davenport, 1961). These established models continue to be employed in contemporary engineering practice (Solari, 2019).

32 Thunderstorm winds known as “downburst” consists of a strong and localized downdraft of air generated within a
33 convective cell. These downdrafts after reaching the ground begins to spread horizontally, resulting in the formation of
34 the downburst gust front, also known as the downburst outflow. The presence of strong turbulent wind within the
35 downburst outflow poses significant risk to civil structures. Given their high frequency of occurrence, downburst events
36 are among the most severe meteorological phenomena in mid latitudes. Downbursts, often generated by isolated
37 thunderstorms, typically exhibit scales of less than few kilometers in extent, distinguishing them from the larger scale of
38 thunderstorms themselves. ~~may be generated by isolated thunderstorms, with length scales less than few kilometers.~~
39 Additionally, they can be originated from more complex convective systems such as squall lines and bow echoes, in this
40 case the spatial length scale which can potentially be affected by downbursts or downburst clusters is in the order of
41 hundreds of kilometers (Fujita, 1978, Hjelmfelt, 2007). The size of the downburst outflow area of strong winds exhibits
42 variability, leading to the classification of this phenomenon as either a microburst or macroburst. A microburst is
43 characterized by a strong outflow size that is less than 4 km, whereas a macroburst corresponds to an outflow size of
44 intense wind greater than 4 km (Fujita, 1985).

45 For over four decades, intense downburst winds and their impact on the built environment have been key research topics
46 in the field of Wind Engineering (Letchford, 2002). These winds, resulting from nonstationary behaviours in mesoscale
47 thunderstorms, create a distinct horizontal wind profile. This profile, marked by a nose-shape with peak wind speed near
48 the ground level, sharply contrast with the typical wind profiles in the ABL and significantly endangers structures,
49 particularly those of low and medium height.

50 ~~For the past four decades, the study of intense downburst wind and their impact on the built environment has constituted~~
51 ~~a prevailing subject of research in the field of Wind Engineering (Letchford, 2002).~~ ~~Since downburst event have high~~
52 ~~frequency of occurrence, they can be considered as one of the most severe meteorological phenomena. Thunderstorm,~~
53 ~~occurring at the mesoscale, exhibit nonstationary behaviour. Their origin is due to an unstable convection condition in~~
54 ~~the atmosphere and the resulting horizontal wind profiles are significantly different from those usually observed in the~~
55 ~~ABL.~~ From a statistical point of view, wind velocities, characterized by a mean return period greater than 10 or 20 years,
56 are often due to these phenomena (Solari, 2014). The lack of a unified model for downburst outflows and their actions on
57 structures, similar to Davenport’s (1961) model for extra-tropical cyclones, is primarily due to significant uncertainties
58 arising by the inherent complexity of downburst winds. Indeed, the transient nature and limited spatial extent of
59 downbursts presents challenges in their measurements and restrict the availability of an adequate number of test cases.

60 The early analytical models for downburst wind velocities stemmed from Glauert's (1956) impinging wall jet model and
61 Ivan's (1986) ring vortex model. Glauert focused on radial jets, while Ivan developed an axisymmetric downburst model
62 validated by the Joint Airport Weather Studies Project (Fujita, 1985; McCarthy et al., 1982), incorporating a primary and
63 mirror vortex above the ground. Oseguera and Bowles (1988) developed the first three-dimensional downburst model,
64 later refined by Vicroy (1991, 1992). This model, simpler yet comparable in effectiveness to Ivan’s (1986) ring vortex
65 model, was based on axisymmetric flow equations and empirical data from the TASS model (Proctor 1987a, b), and
66 NIMROD Project (Fujita, 1978; Fujita, 1985). Holmes and Oliver (2000) revised the impinging jet model, simplifying
67 the expression for radial mean wind velocity and integrating it with the downburst's translational speed. However, their
68 model did not clearly distinguish between the low-level environmental flow in the ABL and the thunderstorm cell's
69 motion. Abd-Elal et al. (2013) used a parametric-CFD model coupled with an optimization algorithm to determine that
70 downburst characteristics are significantly influenced by factors such as the touchdown location, time, and the downdraft's
71 speed and direction. An essential aspect already highlighted with regard to the Holmes and Oliver model (2000), and then

72 repeated in other subsequent papers (Chay et al. 2006, Abd-Elaal et al., 2013, and Hoa Le and Caracoglia (2017), is the
73 lack of a clear distinction between the translational movement of the thunderstorm cell and the boundary layer wind in
74 which the thunderstorm outflow is immersed at the ground. Hjelmfelt's (1988) study through radar measurements
75 highlighted this problem's importance by examining two downbursts. The first case depicted a nearly stationary downburst
76 in strong low-level environmental winds, while the second described a fast-moving downburst in a setting with little or
77 no ABL flow. This lack of distinction in models hinders their ability to accurately describe such diverse real-world cases.

78 Based on these foundational insights provided by Hjelmfelt (1988), the authors of this paper introduced in 2020 a novel
79 bi-dimensional analytical model to simulate the horizontal mean wind velocity at a specific height from a moving
80 downburst (Xhelaj et al. 2020). This model conceptualizes the combined wind velocity at any given point during a
81 downburst as the vector sum of three distinct components: the radial impinging jet velocity characteristic of a stationary
82 downburst, the translational velocity of the storm cell, and the ambient low-level ABL wind velocity, which encompasses
83 the downburst winds near the surface.

84 ~~Xhelaj et. al. (2020) presented an analytical model thought to simulate the bi-dimensional structure of downbursts. The~~
85 ~~model depends on 11 parameters that are estimated using a global metaheuristic optimization algorithm described in~~
86 ~~Xhelaj et. al. (2022). The integration between the analytical model and the optimization algorithm, as well as the~~
87 ~~estimation of the kinematic parameters of the downburst outflow, is based on the Teaching Learning Based Optimization~~
88 ~~(TLBO) algorithm. The TLBO algorithm operates with a population of solutions and emulates a teaching and learning~~
89 ~~activity through iterative process to attain the best solution within the population (Rao et al., 2011). Due to the stochastic~~
90 ~~nature of the TLBO algorithm when coupled with the analytical model, the procedure can produce different optimum (or~~
91 ~~best) solutions each time the algorithm is executed. This variability arises from the initial random population of solutions~~
92 ~~generated at the beginning of the algorithm and the intermediate transformations of the set of solutions carried out by the~~
93 ~~algorithm in order to converge towards the best solution. The model relies on 11 parameters, which are determined using~~
94 ~~a global metaheuristic optimization algorithm outlined in Xhelaj et al. (2022). This optimization process combines the~~
95 ~~analytical model with the Teaching Learning Based Optimization (TLBO) algorithm. TLBO operates with a population~~
96 ~~of solutions and employs iterative teaching and learning to find the best solution within the population (Rao et al., 2011).~~
97 ~~Due to the stochastic nature of TLBO, when integrated with the analytical model, the procedure can yield different optimal~~
98 ~~solutions each time it is executed. This variability arises from the initial random population of solutions and the~~
99 ~~intermediate transformations carried out by the algorithm to converge towards the best solution.~~

100 -This study aims to examine the characteristics of the optimal solutions obtained through multiple runs of the optimization
101 procedure, which integrates the Xhelaj et. al. (2020) model with the TLBO algorithm. It seeks to investigate the variability
102 of the best solutions when applying the optimization algorithm to reconstruct the wind field during an intense downburst
103 event. The main objective is to assess the extent to which the solutions differ from each other and from the solution with
104 the lowest objective function value. Additionally, the study explores whether these alternative solutions can be considered
105 physically valid, particularly when additional data describing the downburst event is incorporated.

106 -The selected downburst event occurred in western Timis region of Romania on 25 June 2021 and was produced during
107 the passage of an intense mesoscale convective system in the form of a bow echo over the town of Sănnicolau Mare, ~~of~~
108 ~~an intense mesoscale convective system of bow echo type~~. This event was recorded by a bi-axial anemometer and
109 temperature sensor, both placed on a telecommunication tower 50 m above the ground level. The telecommunication
110 tower lies approximately 1 km south of Sănnicolau Mare. The downburst that occurred in Sănnicolau Mare was of

111 significant magnitude, resulting in extensive hail damage of the facades of numerous buildings within the city.
112 ~~Subsequent-In response to this event, e-occurrence of this intense event,~~ a comprehensive damage survey was ~~undertaken~~
113 ~~conducted~~ through a collaborative partnership between University of Genoa (Italy) and the University of Bucharest
114 (Romania). The survey (Calotescu et al., 2022 and Calotescu et al., 2023 (submitted)) pinpoints the GPS position of
115 the buildings within the city that were predominantly impacted by the downburst. Moreover, a comprehensive map
116 illustrating the hail damage of the building facades was generated. The map provides important information regarding the
117 wind velocity experienced at urban scale, which has been used to validate the reconstruction/simulation of the downburst
118 by the optimization procedure.

119 The analysis of the different optimal solutions (i.e., the data set) generated by the optimization algorithm was conducted
120 through multivariate data analysis (MDA). This involved the joint application of cluster analysis and principal component
121 analysis to effectively examine and interpret the dataset. Cluster analysis (CA) is a data mining technique that groups
122 similar solutions together, aiming to identify patterns in the data. It is commonly used in fields like meteorology and
123 climatology to identify clusters of weather phenomena or geographical regions with similar weather patterns (Burlando
124 et al., 2008; Burlando et al., 2009). Principal component analysis (PCA) is a mathematical technique used to decrease the
125 dimensionality of a dataset while minimizing the loss of information within the data. This analysis is commonly used in
126 meteorology and climatology to decrease the number of variables required for representing weather pattern or climate
127 trends and to identify regions with similar weather patterns (Amato et al., (2020); Jiang et al., (2020)). Principal
128 component analysis is utilized in this context to enhance the interpretation of the different optimal solutions.

129 The present work is structured in 6 Sections. Following the introduction, Section 2 provides a description of the
130 monitoring system that acquired the full-scale measurement employed in this research. Section 3 provides a brief
131 meteorological description of the downburst event in Sânnicolau Mare (Romania). Section 4 describes the data set
132 employed for performing cluster analysis and principal component analysis as well as the implementation of these
133 analyses. Section 5 presents an in-depth account of the main results derived from the CA and PCA. In conclusion, Section
134 6 offers a summary of the principal findings derived from this research.

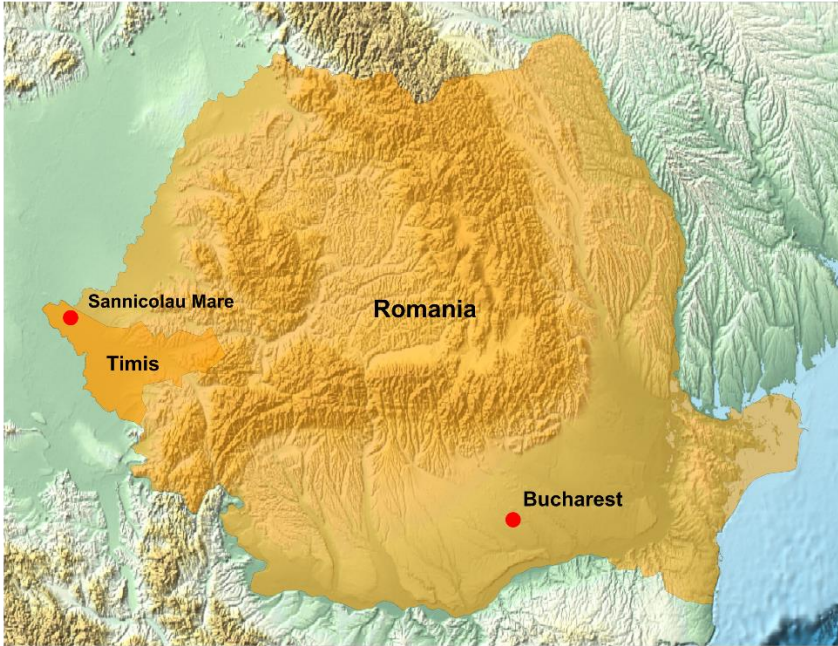
135 **2 Monitoring system and data acquisition**

136 The complete set of measurements employed in this research were obtained through a monitoring system installed in
137 Romania. Relevant information of this monitoring network can be accessed in the publications by Calotescu et al., (2021),
138 Calotescu and Repetto, (2022) and Calotescu et al., (2023) (submitted). The monitoring network received funding from
139 the THUNDERR Project (Solari et al., 2020), which was conducted by the "Giovanni Solari – Wind Engineering and
140 Structural Dynamics" Research (GS-Windyn) Group at the Department of Civil, Chemical, and Environmental
141 Engineering (DICCA) of the University of Genoa. GS-Windyn, with a keen interest in monitoring poles and towers
142 exposed to thunderstorm actions worldwide, secured funding for the acquisition of a full-scale structural monitoring
143 network. This monitoring system was deployed on top of a 50 m lattice tower. The primary focus of this project revolves
144 around three key objectives: first, the detection of thunderstorms; second, the analysis of wind parameters associated with
145 these phenomena; and third, the experimental assessment of the structural response of telecommunication lattice towers
146 to the forces generated by both synoptic and thunderstorm winds. ~~Thunderstorms are local phenomena that occur in~~
147 ~~conditions of atmospheric instability, being characterized by the existence of vertical air currents that lead to the~~
148 ~~development of cumulonimbus clouds, the production of electric discharges, rain, and hail as well as strong downdrafts~~
149 ~~inducing damaging winds in proximity to the Earth's surface. The vertical profile of horizontal wind velocity in downburst~~
150 ~~winds showcases distinct characteristics when compared to the traditional velocity profile observed within the boundary~~

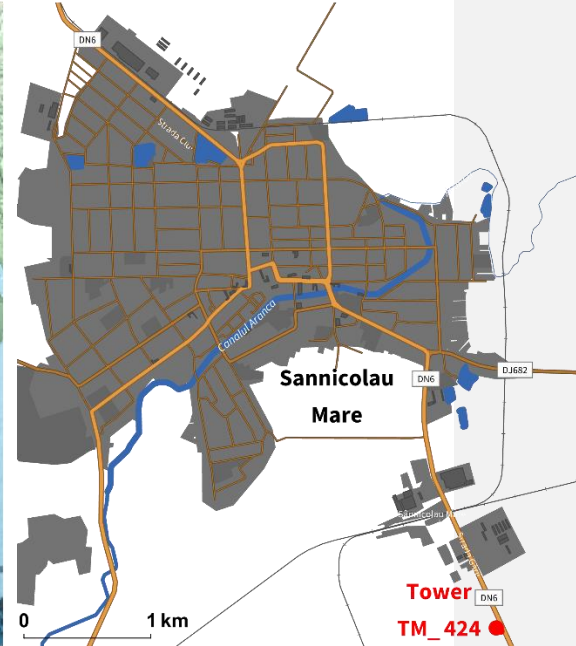
159 layer. Notably, downburst winds exhibit a nose-like shape profile, with a pronounced maximum intensity near the ground.
160 This specific profile presents a considerable risk, particularly for structures of low to medium height. The monitoring
161 tower, named TM_424, is property of the SC TELEKOM ROMANIA SRL and is located in the western part of Romania,
162 Timis county, at approximately 1 km south of Sannicolau Mare (Figure 1Figure 1). The site is an open field, the terrain
163 is flat with low grass vegetation.

ha fo
New

(a)

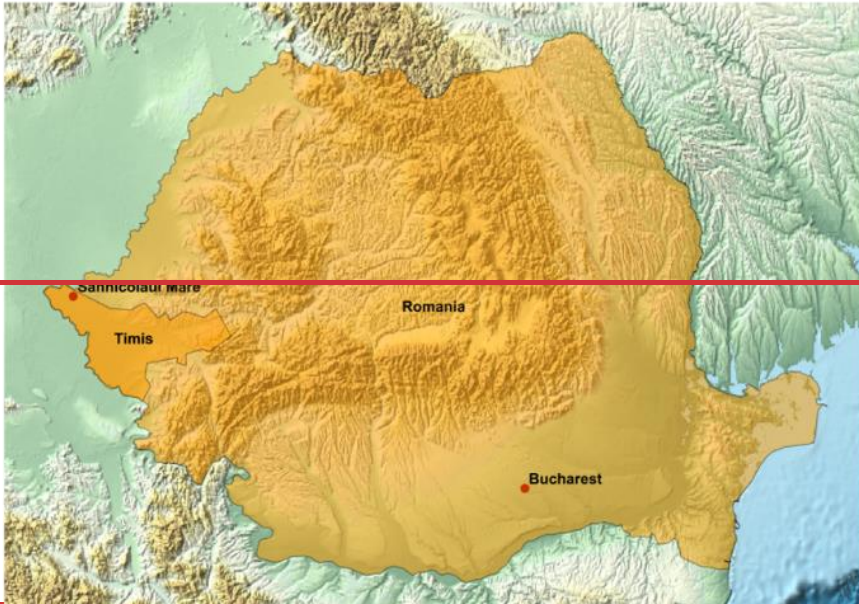


(b)



164

(a)



(b)



165

166

Figure 1. (a) Location of the telecommunication tower TM_424, situated 1 km south of Sânnicolau Mare in Timis County, Romania. (b) Expanded view of the Sânnicolau Mare town with the telecommunication tower TM_424 represented by the red dot on the map. Maps generated using Mathematica (Wolfram Research, Inc., Version 13.3, 2023, <https://www.wolfram.com/mathematica>).

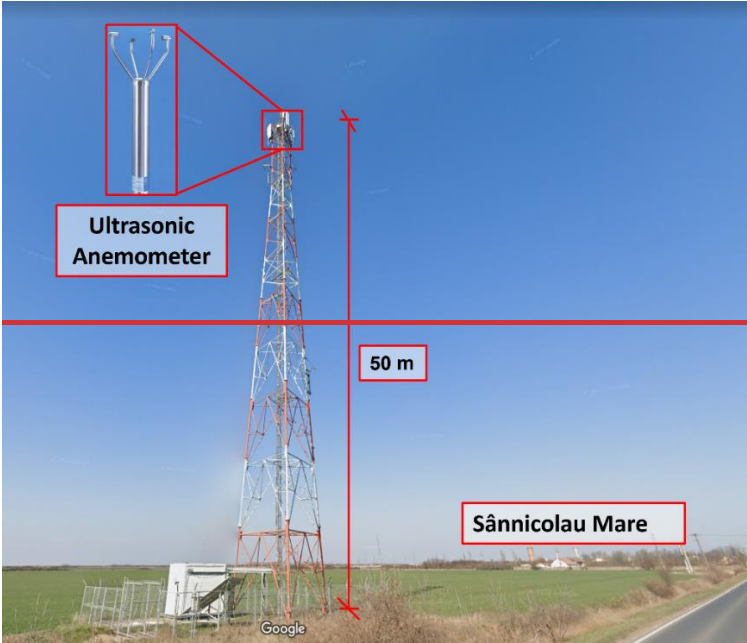
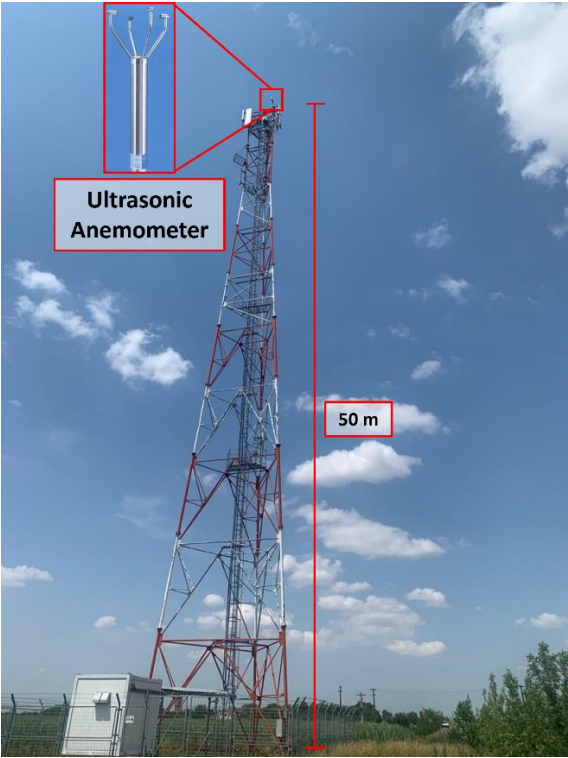


Figure 2. TM_424 Telecommunication tower and sensors position at the top of the tower. On the horizon, approximately 1 km from the tower lies the small city of Sânnicolau Mare. Image courtesy of Google Street View, 2022 (<https://www.google.com/maps>).

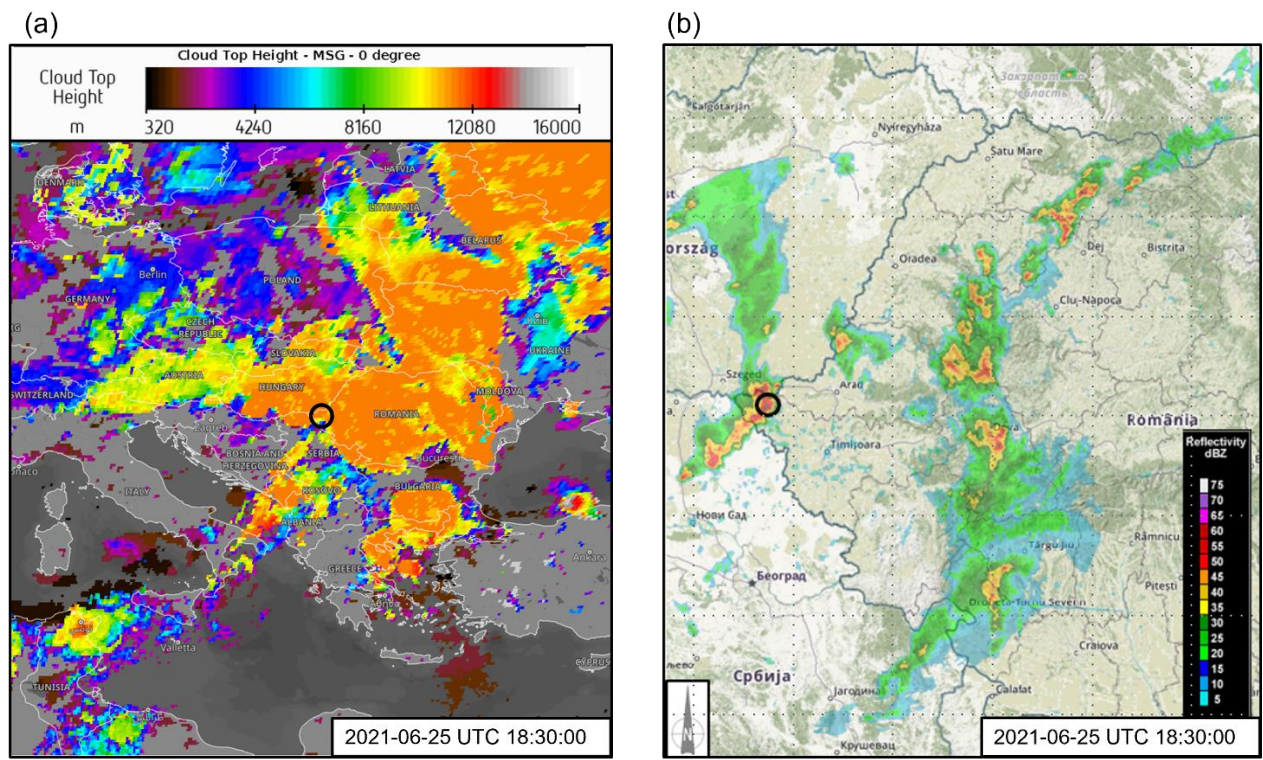
187

188 ~~Figure 2~~ ~~Figure 2~~ shows the dimension of the tower. Among the various networks for the monitoring systems, the tower
 189 is equipped with a GILL WindObserver 70 ultrasonic anemometer at the top (~~Figure 2~~ ~~Figure 2~~). The anemometer has a
 190 data acquisition rate of 4 Hz, can measure the wind speed up to 70 m/s. In addition to the anemometer sensor, the tower
 191 is equipped with a temperature sensor installed near the location of the anemometer. ~~The sensor was encased by a~~
 192 ~~protective case.~~ The working temperature range for this sensor is between -55 and 70 °C.

193

194 **3 The Sânnicolau Mare (Romania) downburst event of 25 June 2021**

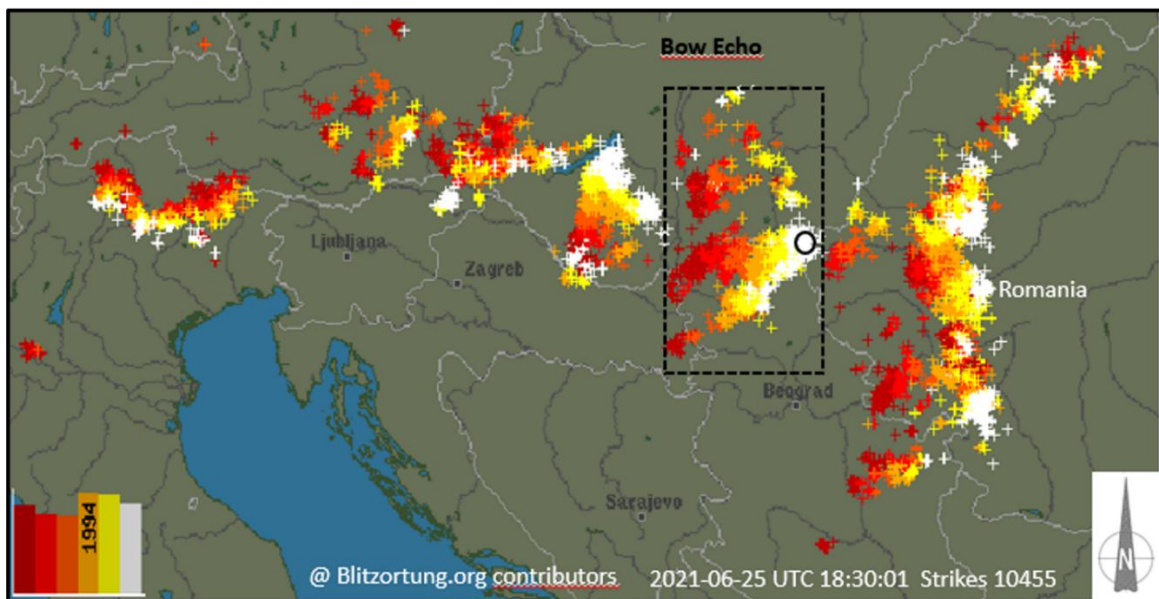
195 In this section, a brief overview of the meteorological aspects pertaining to the downburst event in Sânnicolau Mare on
 196 25 June 2021 is provided. In the late afternoon of 25 June 2021, a severe downburst event affected the extreme western
 197 region of Romania. The downburst event took place in the Timis county (~~Figure 1~~ ~~Figure 1~~a) between 18:00 and 19:00
 198 UTC and struck the little town of Sânnicolau Mare (~~Figure 1~~ ~~Figure 1~~b). At 17:30 UTC, a strong mesoscale convective
 199 system moving toward the east was approaching the town of Sânnicolau Mare. Figure 3a, acquired from Eumetsat,
 200 captures an image of a deep convective cell at 18:30 UTC. This weather phenomenon exhibits cloud tops ascending over
 201 12 km above mean sea level, signifying the mature stage of the convection cycle. This mature storm cell was observed to
 202 have directly impacted the town under study. Figure 3b presents composite radar reflectivity data, indicating that this
 203 meteorological phenomenon can be classified as a mesoscale convective system known as bow echo. Radar reflectivity
 204 values at or above 60 dBZ, as seen in this event, are typically indicative of severe weather conditions. Such conditions
 205 are often associated with the production of hailstones, with an average diameter of approximately 2.5 cm.



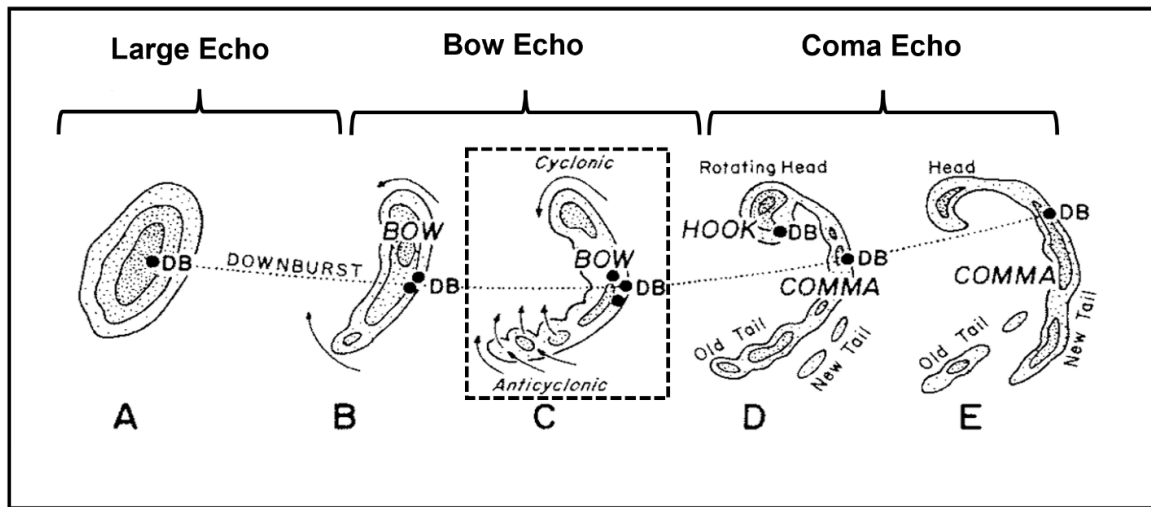
206 **Figure 3. (a) Distribution of cloud top heights derived from Meteosat Second Generation (MSG) valid for 25 June 2021 at 18:30**
207 **UTC. Data and map obtained from ©EUMETSAT 2022 (<https://view.eumetsat.int>). (b) Composite radar reflectivity (dBZ) for**
208 **June 25, 2021, at 18:30 UTC. The geographical location of Sânnicolau Mare and the apex of the bow echo are indicated by the**
209 **black circle. Data and map obtained by ©2018 Administrația Națională de Meteorologie (<https://www.meteoromania.ro>).**

210 The existence of a robust convective motion, indicative of the typical kinematic structure of a bow echo, is distinctly
211 portrayed through the distribution of intensive lightning activity, as displayed in Figure 4a. As the figure illustrates, an
212 approximate total of 10455 lightning strikes were recorded by the Blitzortung.org network across Eastern Europe between
213 16:30 to 18:30 UTC. A significant concentration of these strikes correlates with the bow echo structure near the western
214 Timis County in Romania. The color gradient in Figure 4a, ranging from red, orange, yellow and white serves as a
215 temporal marker, with white color indicating the most recent strikes and with red color denoting older ones. This color
216 coding effectively illustrates the temporal and spatial evolution of the lightning activity during the severe weather event,
217 providing insight into the progression of the storm system. Bow echoes are a prevalent form of severe convective
218 organization. These mesoscale convective systems can generate straight-line surface winds that lead to extensive damage
219 associated with downbursts. On occasion, they may also give rise to tornadoes. Interestingly, the observed bow echo
220 seems to display a stratiform parallel structure, a rarer characteristic variety of squall lines (Parker and Johnson, 2004;
221 Markowski and Richardson, 2010).

(a)

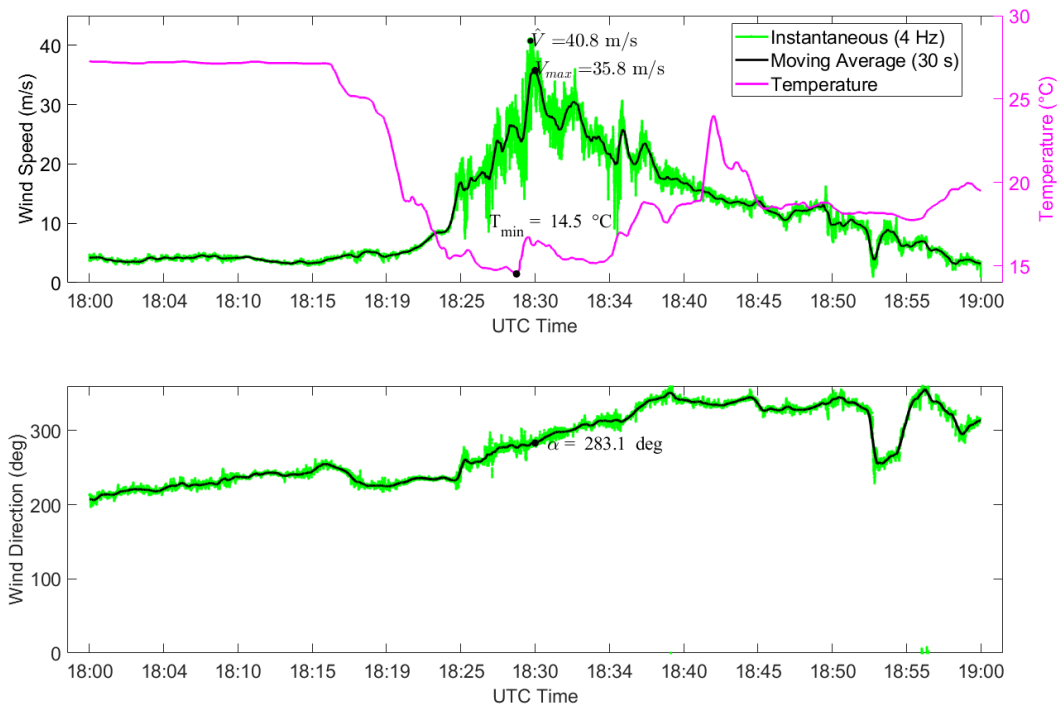


(b)



249 Figure 4. (a) Lightning strikes recorded between 16:30 to 18:30 UTC on June 25, 2021, sourced from the Blitzortung.org
250 network archive for lightning and thunderstorms (www.blitzortung.org). The black circle marks the geographic location of
251 Sânnicolau Mare, situated near the apex of the observed bow echo. (b) Typical radar echo morphology commonly observed in
252 bow echoes, characterized by the generation of strong downbursts at the bow apex, denoted as DB. Adapted from Fujita (1978).

253 Figure 4b illustrates the characteristic kinematic structure of a bow echo as outlined by Fujita (1978). Typically, the
254 system originates as a singular, prominent convective cell, either isolated or embedded within a broader squall line system
255 (Phase A). As the surface winds strengthen, the parent cell undergoes transformation, evolving into a line segment of cells
256 with a bow-shaped configuration (Phase B). During the maximum intensity, the bow's center might develop a spearhead
257 echo (Phase C), characterized by the occurrence of the most severe downburst winds at the apex of the spearhead. During
258 the decay phase, the wind system frequently evolves into a comma-shaped echo (Phase E) (Weisman, 2001). The
259 comparisons between Figures 3b, 4a, and 4b elucidate that the bow echo positioned above Sânnicolau Mare at 18:30 UTC
260 is in its most intense stage (Phase C), as evidenced by the formation of the characteristic spearhead echo shape. The
261 intense downburst event generated at the apex of the bow echo was recorded by the anemometer and temperature sensor
262 situated 50 meters above the ground on the TM_424 tower. The time histories of the moving average wind speed and
263 direction (averaged over 30 seconds) (Solari et al., 2015; Burlando et al., 2017) for the recorded one-hour duration of the
264 downburst event are given in Figure 5a and Figure 5b, respectively. At approximately 18:30 UTC the anemometer
265 recorded an instantaneous maximum velocity (sampled at 4 Hz) of $\hat{V} = 40.8$ m/s while the maximum moving average
266 wind velocity was $V_{\max} = 35.8$ m/s. This notable high velocity clearly evidences of the occurrence of an intense
267 downburst. The time interval spanning from 18:20 to 18:45 UTC represents the primary indicator of the downburst's
268 occurrence in the proximity of the telecommunication tower. This period is characterized by a sudden surge in wind speed,
269 commonly referred intensification stage followed by a subsequent decrease in velocity after 18:30 UTC. Throughout the
270 initial phase of intensification, the wind direction exhibited a clockwise rotation, ranging from 235° and extending to
271 approximately 360° . Additionally, ~~Figure 5~~ [Figure 5a](#) also includes 1-hour time series of the recorded temperature data.
272 The temperature sensor is positioned at the same location of the anemometer. Before the passage of the downburst, the
273 environmental temperature was on average 27°C , while at approximately 18:20 UTC the temperature dropped very
274 sharply reaching the minimum value of 14.5°C at approximately 18:30 UTC. After the sharp drop the temperature started
275 to rise and eventually returned to its pre-storm level (not shown).



276

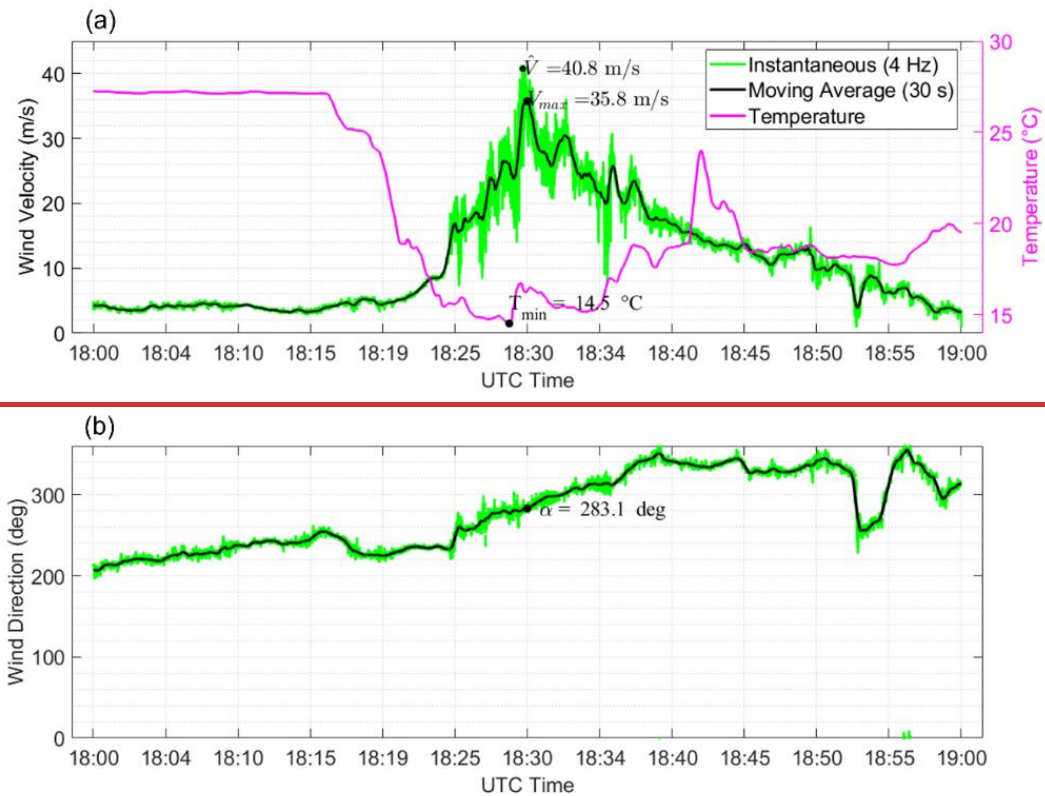
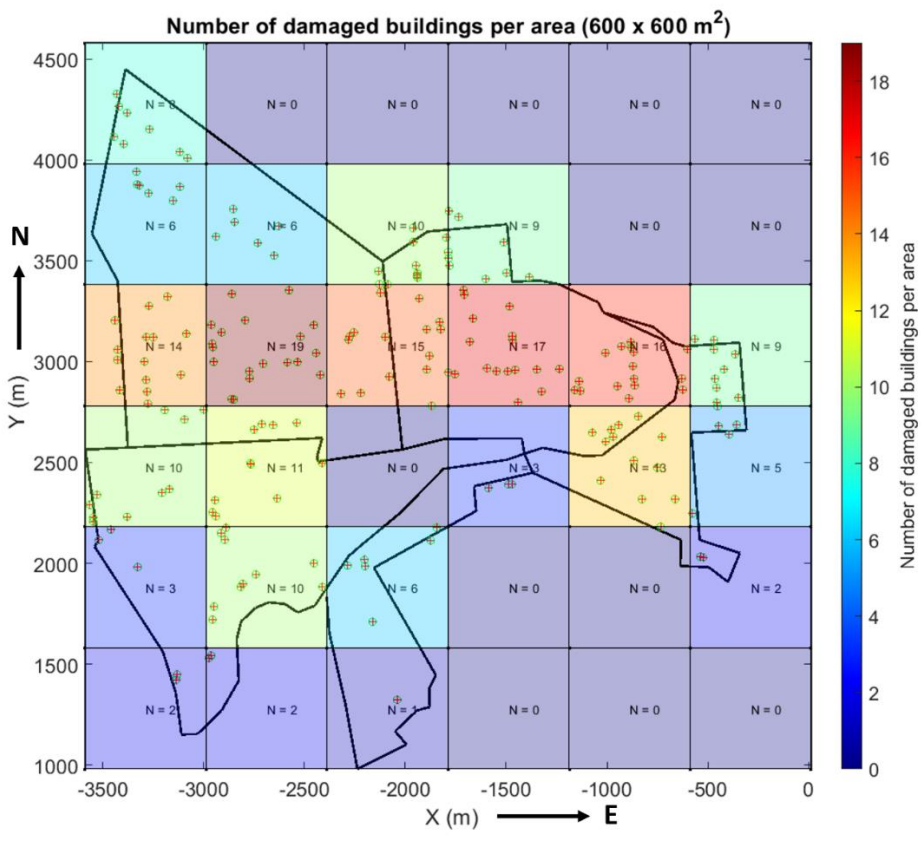


Figure 5. Telecommunication tower monitoring network measurements from 18:00 to 19:00 UTC on June 25, 2021: (a) Time history of the instantaneous wind speed (green), moving average mean wind speed (black) and temperature record (magenta); (b) Instantaneous (green) and moving average mean wind direction (black).

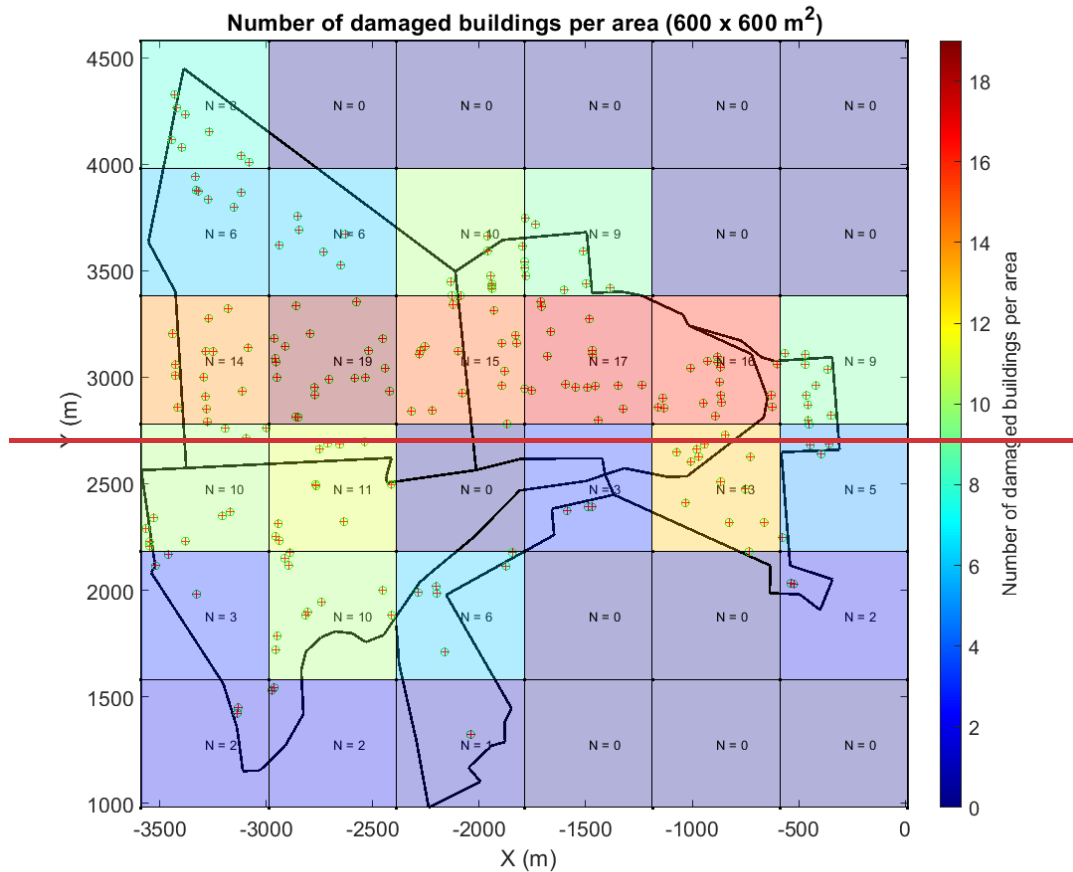
277

291 The downburst in Sânnicolau Mare, primarily a significant wind event, was also marked by a substantial hail occurrence.
 292 The interaction between the high-velocity winds and hail, potentially influencing the trajectory and impact of the
 293 hailstones, contributed to extensive damage, especially to the facades of numerous buildings. The downburst in Sânnicolau
 294 Mare caused widespread hail damage to the facades of numerous buildings. To comprehensively assess this damage, a
 295 collaborative survey was conducted by the University of Genoa (Italy) and the University of Bucharest (Romania)
 296 (Calotescu et al., 2022; Calotescu et al., 2023, submitted). A collaborative damage survey was conducted by the University
 297 of Genoa (Italy) and the University of Bucharest (Romania) (Calotescu et al., 2022; Calotescu et al., 2023, submitted).
 298 The survey identified the affected buildings and produced a comprehensive map illustrating the hail damage. Figure
 299 6 shows a schematic representation of the distribution of hail damage per area (600 x 600 m²) and the position of
 300 the buildings that suffers hail damage in the town of Sânnicolau Mare. Correlating specific damages like hail impacts
 301 with near-surface wind velocities involves inherent uncertainties, which are extensively explored in the study by
 302 Calotescu et. al., 2023 (submitted).

ha fo
New



303



304

Figure 6. Spatial distribution of damaged buildings and locations of hail-damaged structures within 600 x 600 m² area in the town of Sânnicolau Mare during the downburst event on June 25, 2021. The city boundaries of Sânnicolau Mare are delimited by the black line.

305 **4 Downburst reconstruction**

306 This section focuses on the modeling, optimization, and reconstruction of the Sânnicolau Mare downburst event. Section
 307 4.1 delves into the modeling and optimization approach used for downburst reconstruction. Section 4.2 introduces
 308 metaheuristic optimization and its application in the reconstruction of the specific downburst event under study. Finally,
 309 Section 4.3 outlines the multivariate data analysis employed to examine the solutions generated by the optimization
 310 algorithm.

311 **4.1 Modeling and optimization approach for downburst reconstruction**

312 In this study, the authors utilize the computational model developed in a previous work by Xhelaj et al. (2020) for the
 313 reconstruction and simulation of the Sânnicolau Mare downburst event discussed in Section 3. The Xhelaj et al. (2020)
 314 model can simulate the spatiotemporal evolution of the bi-dimensional moving average (30 second window) wind speed
 315 and direction experienced during a typical downburst event at a specified height z above ground level (AGL). ~~The Xhelaj
 316 et al., (2020) model is able to reconstruct/simulate the space-time evolution of the bi-dimensional moving average wind
 317 speed and direction produced during a generic downburst event at a height z above the ground level (AGL). The wind
 318 system simulated by the model represents the outflow structure of a translating downburst embedded in a synoptic scale
 319 wind, which is considered as constant across the simulation domain. In general, the wind system simulated by the
 320 analytical model represents the outflow structure of a translating downburst, typically occurring in diverse meteorological~~

348 conditions such as single cell thunderstorms, multicell thunderstorms, squall lines and bow echoes. For the specific case
 349 of the Sânnicolau Mare downburst, the analytical model operates under the hypothesis that the downburst occurs near the
 350 tip of the bow echo during its mature stage (Phase C, Figure 4b), in line with the studies of Fujita (1978) and Weisman
 351 (2001). It is worth noting that the model does not encompass the broader, complex mesoscale circulations, commonly
 352 associated with high winds in bow echoes. This represents a focused approach, considering the downburst evolution
 353 within a specific context, rather than attempting to model the entire spectrum of atmospheric phenomena related to bow
 354 echoes.

355 The analytical model comprises 11 variables that describe the kinematic structure of the downburst wind. Table 1
 356 † presents a short description of the 11 variables upon which the model relies. As a result, the model allows for the
 357 reconstruction of the time-evolving moving average wind speed and direction generated by the simulated downburst at
 358 every point within the simulation domain. The model simulates the downburst wind velocity field by combining three
 359 components, the stationary radial velocity from a jet impacting a flat surface, the downdraft’s translation velocity (i.e.,
 360 storm motion) and the low level ABL wind velocity. The virtual anemometer, situated at the center of the simulation
 361 domain, measures the simulated wind speed and direction generated by the model. By employing anemometric wind
 362 speed and direction data collected during the Sânnicolau Mare downburst event, an optimization procedure can be
 363 formulated to minimize the relative error (objective function F), which quantifies the discrepancy between the observed
 364 time series of the moving average wind speed and direction and the corresponding simulations generated by the model.
 365 Since the Sânnicolau Mare downburst event was recorded by an anemometer positioned at a height of 50 meters AGL,
 366 the analytical model will reconstruct the wind speed and direction at the corresponding height.

367 **Table 1. Variables of the Xhelaj et., al. (2020) analytical model.**

1	X-component touchdown location (at $t = 0$) (m)	X_{C0}
2	Y-component touchdown location (at $t = 0$) (m)	Y_{C0}
3	Downdraft radius (m)	R
4	Normalized radial distance from the center of the downburst where $V_{r,max}$ occurs (-)	$\rho = \frac{R_{max}}{R}$
5	Maximum radial velocity (m/s)	$V_{r,max}$
6	Duration of the intensification period (min)	T_{max}
7	Total duration of the downburst event (min)	T_{end}
8	Storm translational velocity (m/s)	V_t
9	Storm translational direction (deg)	α_t
10	ABL wind speed below the cloud base (m/s)	V_b
11	ABL wind direction below the cloud base (deg)	α_b

368
 369 The reconstruction procedure gives rise to a mathematical optimization problem characterized by being single-objective,
 370 nonlinear, and bound constrained, as discussed in Xhelaj et al. (2022). To tackle this optimization problem, the analytical
 371 model is integrated with a global metaheuristic optimization algorithm. Specifically, the Teaching Learning Optimization
 372 Algorithm (TLBO) proposed by Rao et al. (2011) is employed. The details pertaining to the integration of the analytical
 373 model with the optimization algorithm, as well as the estimation of the kinematic and geometric variables associated with
 374 the downburst event, are explained in detail in Xhelaj et al. (2022). The TLBO algorithm † is an iterative, stochastic, and

375 population-based algorithm comprising two distinct phases: the Teacher Phase and the Learner Phase. In the Teacher
 376 Phase, the best solution in the population (the teacher) shares its knowledge (objective function) with the other solutions
 377 (the students) to enhance their performance. In the Learner Phase, the students interact with each other to further improve
 378 their performance. TLBO requires only two user-specified parameters: the maximum number of iterations T and the
 379 population size N_p . When incorporating the objective function into a stochastic metaheuristic optimization algorithm,
 380 running the algorithm independently multiple times is crucial to reach the optimal solution. This iterative approach allows
 381 for a deeper exploration of the variable space, reducing the risk of getting trapped in local optima. However, it is important
 382 to note that in the context of metaheuristic optimization, there is no guarantee of attaining a globally optimal solution. As
 383 a result, the procedure can yield a range of solutions ordered based on the values assumed by the objective function, with
 384 some being better than others. In this study, the TLBO algorithm is executed 1024 times independently, with each run
 385 producing an optimal solution. Consequently, 1024 solutions are obtained. The reconstruction of the downburst event can
 386 be accomplished by selecting the solution with the lowest objective function value, as it is considered the best
 387 representation of the event based on the optimization process. This study aims to analyze and clarify the nature of all the
 388 solutions generated by means of the TLBO algorithm for the downburst outflow reconstruction. This choice was made
 389 for a twofold reason.

- 390 • The first reason is to determine the best possible solution among the 1024 totals, where best solution is the one
 391 that minimizes the objective function F , and allows to reconstruct the Sânnicolau Mare downburst event.
- 392 • The second reason, which is the primary objective of this study, is to analyze these 1024 solutions using
 393 multivariate data analysis (MDA). The method used in MDA are the Agglomerative hierarchical clustering
 394 (AHC) coupled with the K-Means algorithm and principal component analysis (PCA).

395 The objective is to investigate the distinct characteristics of the different solutions provided by the TLBO algorithm,
 396 enabling an understanding of their divergence from the optimal solution. If alternative solutions do exist, it signifies that
 397 the algorithm's solution is not unique. This highlights the challenge in accurately reconstructing downburst wind field
 398 form just one anemometric time series, underlining the problem's inherent complexity and underdetermined nature.—As
 399 such, a more comprehensive definition of the objective function is necessary to accurately discern between the optimal
 400 solution and its alternatives.

401 4.2 Metaheuristic optimization and reconstruction of the Sânnicolau Mare downburst

402 In metaheuristic optimization, a commonly used guideline suggests setting the population size N_p as ten times the number
 403 of variables to estimate D (Storn, 1996). In this study, where D corresponds to 11 variables, a population size of $N_p = 110$
 404 has been chosen. Additionally, considering the reported fast convergence rate of the TLBO algorithm (as mentioned in
 405 Xhelaj et al., 2022), the maximum number of iterations T for this study has been set to $T = 100$. Table 2 displays the lower
 406 and upper bounds of the optimization problem pertaining to the reconstruction of the Sânnicolau Mare downburst. These
 407 parameter values have been determined based on a comprehensive literature review, available in Xhelaj et al. (2022).

409 **Table 2. Lower and upper bound of the decision variable parameters for the reconstruction of the Sânnicolau Mare**
 410 **downburst. Table form Xhelaj et al. (2022).**

	Parameters/Variables	Lower Bound	Upper Bound
--	----------------------	-------------	-------------

1	X_{C0} (m)	-10000	-10000
2	Y_{C0} (m)	-10000	-10000
3	R (m)	200	2000
4	$\rho = \frac{R_{max}}{R}$ (-)	1.6	2.6
5	$V_{r,max}$ (m/s)	0	40
6	T_{max} (min)	2	15
7	T_{end} (min)	15	60
8	V_t (m/s)	0	40
9	α_t (deg)	0	359.9
10	V_b (m/s)	0	40
11	α_b (deg)	0	359.9

440

441

442

443

444

445

446

447

448

449

450

451

452

453

454

455

456

457

458

459

460

461

462

463

464

465

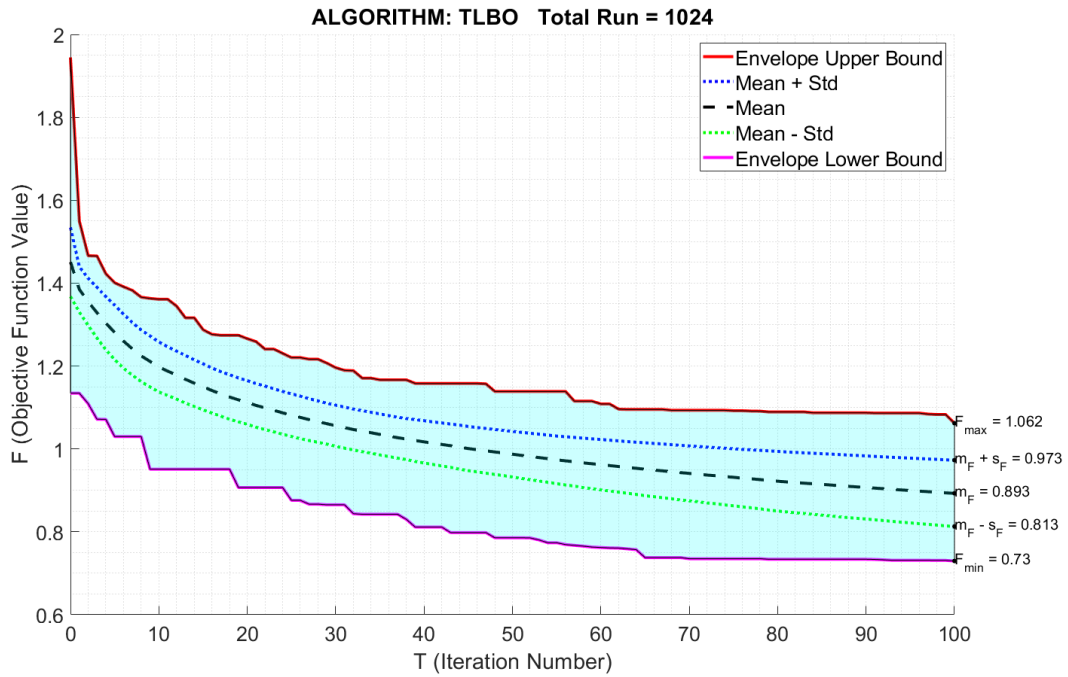
466

467

468

The spatial domain of the downburst simulation covers an area of 20 x 20 km² while the grid resolution in both the X and Y directions is set at 50 m. ~~At the center of the domain is placed the probe that sense the time histories of the wind velocity and direction due to the passage of the simulated downburst.~~ This approach employs a comprehensive simulation approach, primarily using anemometric data, due to its common availability. The methodology entails numerous simulations to extract downburst's kinematic and geometric parameters. However, when additional data like Radar or Lidar is available, this information can be used to bound some variables ~~the reconstruction methods adapts, integrating these information to refine and restrict the model variables domain (Table 2) and to enhance model accuracy.~~ Figure 7 illustrates the "performance chart" depicting the convergence pattern of the objective functions during the reconstruction of the Sănnicolau Mare downburst using the TLBO algorithm. The performance chart in Figure 7 illustrates the convergence pattern of the objective functions as iterations progress. It shows the upper and lower envelopes that encapsulate all 1024 independent runs. The region within the envelopes represents the objective function values' trend for all runs. At the end of the 100 iterations, the lower envelope represents to the best objective function value obtained, while the upper envelope corresponds to the worst objective function value obtained by the TLBO algorithm. The performance chart in Figure 7 includes additional visual representations: a dashed line representing the mean convergence curve, and dotted lines representing the mean plus/minus one standard deviation curves. These curves provide insights into the average behavior and deviation of the objective function values across the 1024 runs. ~~The performance chart demonstrates that after approximately 70 iterations, the TLBO algorithm ceases to find significantly better or worse solutions. This is evidenced by the convergence of both the upper and lower envelope curves. Concurrently, the mean curve appears to plateau, although it exhibits a slight yet continuous improvement beyond the 70th iteration. This suggests that the algorithm is still optimizing, albeit at a reduced rate. The increasing spread between the mean and the plus/minus one standard deviation curves as iterations progress indicates a complex solution landscape. This complexity is manifested in the algorithm's convergence to various local minima, maintaining steady average performance while increasing the variability of solutions. In this study's context, such expanding spread represents a deeper and more intricate exploration of the solution space, a desirable characteristic to ensure a comprehensive search across the objective function domain. Based on the analysis of the performance charts, it can be observed that the TLBO algorithm attains convergence after approximately 70 iterations.~~ At the conclusion of 100 iterations, the best and worst objective function values correspond to $F_{min} = 0.730$ and $F_{max} = 1.062$, respectively. The mean and standard deviation of the objective function values are determined as $m_F = 0.893$ and $s_F = 0.080$, respectively.

ha fo
New



469

470 **Figure 7. Performance chart for the reconstruction/simulation of the Sânnicolau Mare downburst using the TLBO algorithm.**

471

472 4.3 Multivariate data analysis of solutions for the Sânnicolau Mare downburst reconstruction

473 The optimization algorithm provides in output a data table, where each row of the table is a solution of the optimization
 474 problem. Therefore, the data table is composed of 1024 rows (solutions). The table has 12 columns, where 11 columns
 475 represent the 11 variables/parameters of the analytical model, while the last column contains the values assumed by the
 476 objective function F of each solution (i.e., each row). Although the objective function F , is not a variable of the analytical
 477 model, it is treated in Section 5 as a variable from the point of view of the multivariate data analysis. The solutions are
 478 sorted in descending order based on their objective function value F . This means that the best overall solution among the
 479 1024, lies in the last row of the data table. The analysis of the data table indicates that most variables exhibit multimodal
 480 histograms, with two or more peaks. However, only the variables V_b and α_b are characterized by a unimodal histogram.
 481 Since the aim of this document is to conduct a multivariate data analysis (MDA), the variables of the data table are split
 482 into primary and secondary variables. Primary variables participate in the analysis of multivariate data (i.e., AHC + K-
 483 Means and PCA), as opposed to secondary variables, which have no role in the calculation. However, secondary variables
 484 can indeed assist in the interpretation of the data table. In the present study, V_b , α_b and α_t are considered as secondary
 485 variables. This choice is primarily driven by the observation that V_b , and α_b exhibit unimodal histograms, suggesting that
 486 they may not significantly contribute to distinguishing different cluster solutions. However, the choice of α_t as a
 487 secondary variable is purely practical, since it makes it possible to carry out a multivariate statistical analysis, avoiding
 488 the problem of circular statistics and, hence, simplifying the calculation and the interpretations of the results.

489

490 Let's define the data table that contains only primary variables by a matrix \mathbb{X} . Each row i of the matrix represents a
 491 solution vector \mathbf{X}_i , encompassing the values associated with the nine primary variables. Therefore the solution vector can

492 be expressed as $\mathbf{X}_i = (X_{C0_i}, Y_{C0_i}, R_i, \rho_i, V_{r,max_i}, T_{max_i}, T_{f_i}, V_{l_i}, F_i)^T$ with i ranging from 1 to I , where I represents the
 493 total number of solutions, in this case $I = 1024$. Since the solution vector \mathbf{X}_i contains $K = 9$ primary variables, the
 494 resulting data matrix \mathbb{X} is an I -by- K matrix with 1024 rows and 9 columns. For the sake of simplicity, in order to shorten
 495 the notation, let X_{ik} be the value of the k -th primary variable in the i -th solution. Henceforth, the term “variable” will
 496 refer to primary variables, unless explicitly specified. Consequently, the dataset within the matrix \mathbb{X} can be regarded either
 497 as a collection of rows representing solutions to the optimization problem or as a collection of columns representing
 498 variables of the analytical model. ~~The focus of the MDA lies in examining the data matrix from both the solution and~~
 499 ~~variable perspectives, aiming to identify similarities among solutions based on their variables. In essence, the goal is to~~
 500 ~~establish a typology of solutions by identifying groups that exhibit homogeneity in terms of variable similarity. The focus~~
 501 ~~of MDA is to apply statistical clustering to identify similar analytical solutions. This analysis allows for a comprehensive~~
 502 ~~understanding of the relationships and patterns among the solutions, facilitating the identification of distinct solution~~
 503 ~~clusters based on their shared variable characteristics.~~ Since a generic solution \mathbf{X} , is a set of $K = 9$ numerical values, \mathbf{X}
 504 evolves within a space \mathbb{R}^K (a space with 9 dimensions), called “the solution’s space”. Defining in the solution’s space the
 505 usual Euclidean metric (i.e., the l_2 norm $\|\cdot\|_2$), then, the squared distance between two solutions \mathbf{X}_i and \mathbf{X}_l can be
 506 expressed by the Euclidean distance d_{il} :

$$d_{il}^2 = d^2(\mathbf{X}_i, \mathbf{X}_l) = \|\mathbf{X}_i - \mathbf{X}_l\|_2^2 = \sum_{k=1}^K (X_{ik} - X_{lk})^2 \quad (1)$$

507 The distance d possesses the following metric properties:

$$\begin{cases} d(\hat{\mathbf{X}}_i, \hat{\mathbf{X}}_l) = 0 & \Leftrightarrow i = l \\ d(\hat{\mathbf{X}}_i, \hat{\mathbf{X}}_l) = d(\hat{\mathbf{X}}_l, \hat{\mathbf{X}}_i) & \text{(symmetry)} \\ d(\hat{\mathbf{X}}_i, \hat{\mathbf{X}}_l) \leq d(\hat{\mathbf{X}}_i, \hat{\mathbf{X}}_j) + d(\hat{\mathbf{X}}_j, \hat{\mathbf{X}}_l) & \text{(triangle inequality)} \end{cases}$$

509 ~~The Euclidean distance not only enables distance calculations but also allows for the definition of angles and,~~
 510 ~~consequently, orthogonal projections. This concept is fundamental in principal component analysis since PCA relies on~~
 511 ~~the Euclidean distance as a key component of its methodology. Variables in the data matrix~~ Conducting the analysis
 512 ~~directly on the data matrix \mathbb{X} are standardized to account for different units and scales. This common practice in statistical~~
 513 ~~modelling neutralizes scale effects allowing for meaningful comparisons across variables. could be misleading without~~
 514 ~~any kind of standardization or normalization. Standardization of the data is essential, particularly when variables are~~
 515 ~~expressed in different units (refer to Table 1), as it ensures comparability and removes the influence of scale variations.~~
 516 ~~Additionally, even when variables share the same units, disparities in the range of variability can skew the analysis.~~
 517 ~~Therefore, normalization operations become crucial to provide equal weight and significance to each variable, which~~
 518 ~~ultimately leads to a more comprehensive understanding of the data’s structure and relationships. Therefore, in the present~~
 519 ~~work~~ the variables are standardized according to the following equation:

$$\hat{X}_{ik} = \frac{X_{ik} - \bar{X}_k}{S_k}, \quad \forall i = 1, \dots, I = 1024 \quad \text{and} \quad \forall k = 1, \dots, K = 9 \quad (2)$$

520 where \bar{X}_k denotes the sample mean of the k -th variable calculated over all I solutions: $\bar{X}_k = \frac{1}{I} \sum_{i=1}^I X_{ik}$ and S_k is the

521 sample standard deviation of k -th variable: $S_k = \sqrt{\frac{1}{(I-1)} \sum_{i=1}^I (X_{ik} - \bar{X}_k)^2}$.

540 From a geometric standpoint, the standardization operation holds meaningful interpretations within the solution's space
 541 \mathbb{R}^K . The centring operation $X_{ik} \rightarrow \bar{X}_k$ is equivalent to relocating the origin of the reference system to the centre of mass
 542 of the point cloud. The centre of mass coordinates, \bar{X}_k (for $k = 1, \dots, K$), represent the new origin. The standardization
 543 operation, which consists of considering \hat{X}_{ik} rather than X_{ik} , modifies the cloud's shape harmonizing its variability across
 544 all directions. Finally, the normalized data matrix $\hat{\mathbb{X}}$ containing the set of vectors $\hat{\mathbf{X}}_i$, $i = 1, \dots, I$, has been used in the
 545 MDA for the identification of different typology of solutions provided by the TLBO algorithm for the
 546 simulation/reconstruction of the Sănnicolau Mare downburst. Figure 8 showcase a summary statistic in the form
 547 of a box plot, illustrating the distribution of the standardized variables. Variables such \hat{R}_{max} and \hat{T}_{max} have a large
 548 number of outliers which indicates extreme values within the dataset. Therefore, even in the context of standardized data,
 549 outliers can still be informative and may hold important information for distinguishing distinct solution clusters.

ha fo
New

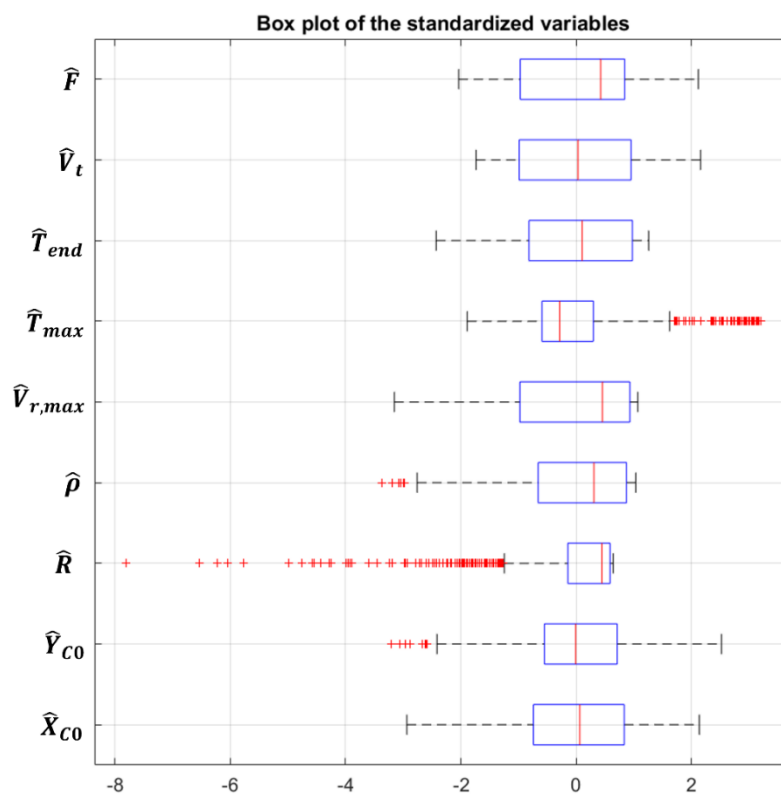


Figure 8. Box plot of the distributions of the standardized variables. Outliers in the data are plotted individually using the red marker symbol + .

550 5 Results

551 In the following section the results of multivariate data analysis (MDA) including cluster analysis and principal
 552 component analysis applied to the data matrix $\hat{\mathbb{X}}$ is presented. After the clusters have been established a comprehensive
 553 description of each of them is provided. This involves examining the variables that contribute to each cluster's composition
 554 as well as identifying specific representative solutions within each cluster. Such an analysis allows for a deeper
 555 understanding of the cluster characteristics and facilitates the interpretation of meaningful patterns and insights within the
 556 data. Sections 5.1 to 5.3 provide an in-depth analysis of data matrix $\hat{\mathbb{X}}$ from the variable's perspective, employing
 557 agglomerative ~~hierarchical~~ hierarchical ~~K~~ - Mmeans clustering and principal component analysis. In Section 5.4 the

595 clusters are analyzed from the point of view of the specific solutions which are the most representative of the clusters.
596 Finally, these representative solutions are compared with the best overall solution founded from the TLBO algorithm.
597 The comparisons of the representative solution for each cluster and the best overall solution with the full-scale data is
598 therefore enriched considering the data from the damage [campaign-survey](#) that was carried out after the Sânnicolau Mare
599 downburst event.

600 5.1 Identification of the most meaningful clusters

601 In order to identify the appropriate number of clusters for grouping the solutions, the agglomerative hierarchical clustering
602 (AHC) is firstly employed (Hartigan, (1975), Kaufman and Rousseuw (1990)). In AHC, each individual solution is
603 initially treated as an independent cluster (leaf). Through a series of iterative steps, the most similar clusters are
604 progressively merged, forming a hierarchical tree structure known as a dendrogram. This merging process continues until
605 all the individual clusters are combined into a single cluster (root).

606 -Subsequently, the hierarchical tree is analysed, and a suitable level is chosen to cut the tree, leading to distinct and
607 meaningful clusters. The number of clusters obtained from the AHC forms a partition of the data set. To refine and
608 optimize this partition, a partitioning clustering algorithm called K-means (MacQueen, 1967, Hartigan and Wong, 1979)
609 is subsequently applied. Partitioning algorithms, like K-Means, subdivides the data sets into distinct clusters, ensuring
610 that solutions within each cluster are similar to one another while exhibiting noticeable differences between clusters.
611 Hence the two steps clustering procedure is called agglomerative hierarchical K – means clustering (AHK-MC) and is
612 employed to analyse the standardized data matrix \hat{X} . By combining the strengths of both algorithms AHC and K-means,
613 AHK-MC aims to provide a comprehensive and improved clustering algorithm of the data, enabling a more accurate
614 identification of distinct solution groups.

615 -The hierarchical tree [in Figure 9](#) (i.e., dendrogram) is constructed following the Wards' method (Ward, (1963)). [Figure](#)
616 ~~9 shows the structure of the dendrogram obtained according to the Wards' algorithm.~~ Since the total solutions of the
617 optimization problem are $I = 1024$, the dendrogram is very dense at the bottom level (i.e., at the leaf level, where each
618 solution is considered as a cluster by itself). The hierarchical tree is composed therefore by $I - 1 = 1023$ nodes, the
619 points where two clusters (solutions or set of solutions) are merged. The level (height) of each node in the tree is described
620 by the within-cluster variance. The level of a node in the agglomeration process, when examined from top to bottom,
621 indicates the reduction in within-cluster variance achieved by merging two connected clusters. This reduction in variance
622 can be visualized using a bar graph, as depicted in Figure 10.

623 -From [Figure 10](#) ~~Figure 10~~ it is possible to establish the level where to cut the dendrogram and consequently to establish
624 the number of clusters for partitioning the data set. The choice of the number of clusters is important because partitioning
625 with too few clusters risk leaving groups which are not at all homogeneous. On the other hand, partitioning with too many
626 clusters' risks creating classes that are not very different from each other. Being $\sum_{s=1}^{I-1} \Delta_s = K = 9$ (the total variance
627 contained in the standardized data), the separation into two groups is able to describe $\Delta(1,2)/K = 4.314/9 = 0.4793$
628 (47.93 %) of the total variance. Considering the partitioning into three groups, the explained variance by the three clusters
629 is equal to $[\Delta(1,2) + \Delta(2,3)]/K = [4.314 + 1.044]/9 = 0.5954$ (59.54 %) of the total variance, while for four clusters
630 the “explained variance” is equal to $[\Delta(1,2) + \Delta(2,3) + \Delta(3,4)]/K = [4.314 + 1.044 + 0.406]/9 = 0.6404$
631 (64.05 %) of the total variance.

645 Therefore, considering more than three clusters (refer to Figure 10~~Figure 10~~) is going to have a very little impact on the
646 explained variance since very little information is gained and is no longer useful to group together any more classes. For
647 this reason, the dendrogram in this work is partitioned in 3 clusters (refer to Figure 9) and therefore they can explain
648 approximately 60% of the total variance present in the data.

649 -The three-cluster solution's ability to explain about 60% of the total variance is significant, especially considering the
650 single-point (anemometric) measurement nature of the downburst data. This inherent limitation often leads to high
651 variability, making the extraction of consistent patterns challenging. As noted in related studies, such as those by
652 Bogensperger and Fabel (2021), benchmarks for acceptable levels of explained variance in clustering are not universally
653 applicable but rather depend on the specific context and data characteristics. The present study's level of variance
654 explanation, given the complexity and variability of the downburst captured from one location, is therefore robust. This
655 is further supported by the observation in Figure 10 that additional clusters contribute minimally to the total variance
656 explained, suggesting that the primary structural patterns in the data are adequately captured with three clusters.

657

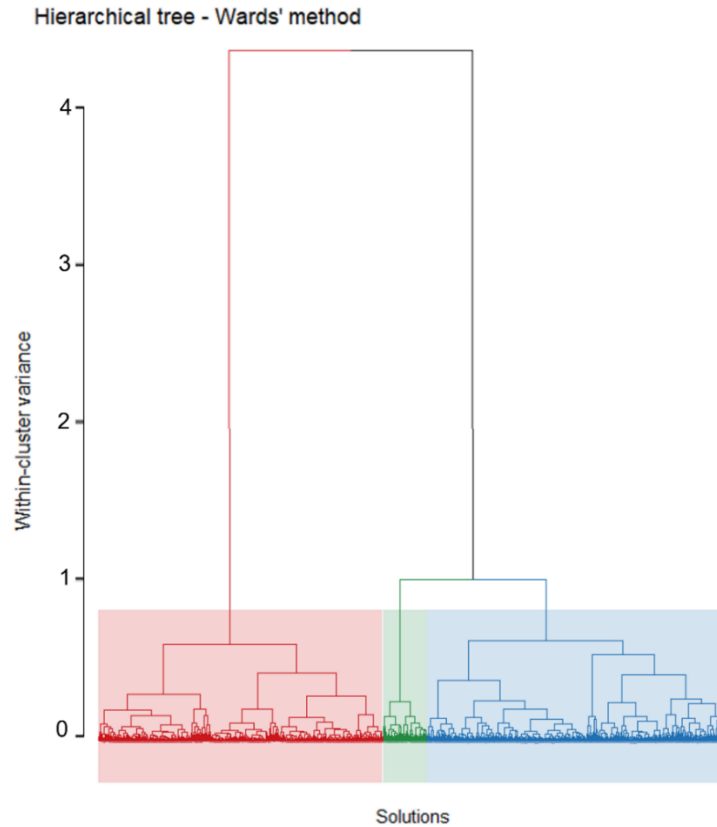
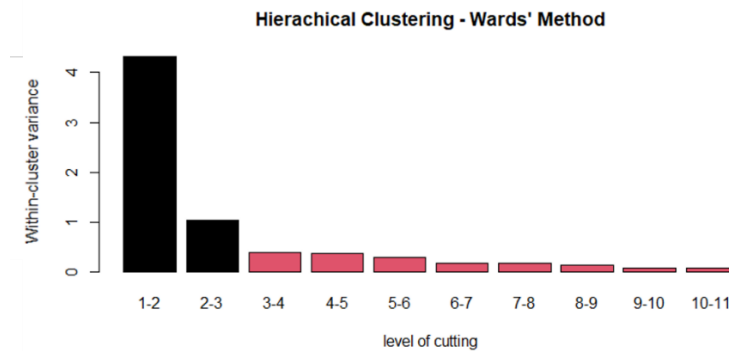


Figure 9. Hierarchical tree (dendrogram) created with Ward's Method, categorizing the optimization problem solutions for the Sânnicolau Mare downburst into three clusters, each marked by a distinct color: red for cluster 1, green for cluster 2, and blue for cluster 3.

658



659 Figure 10. Bar graph of the relation between the number of merged clusters and the within-cluster variance.

660 **5.2 Interpretation of the clusters through pea and optimization using k-means**
 661 **Clusters interpretation via PCA and Optimization with K-Means**

662 The three clusters of solutions are analyzed using principal component analysis (PCA) to identify the key variables that
 663 drive the system's behavior. By extracting the principal components, which captures the most significant variation in the
 664 data, the complexity of the system can be reduced. In particular, the eigenvalues of the correlation matrix $S = \frac{1}{(I-1)} \hat{X}^T \hat{X}$
 665 quantify the amount of variance accounted by each principal component (Kassambara, 2017). The eigenvalues shows that

700 the first components have larger values, indicating that they capture the most significant variation in the data set. In
701 contrast, the subsequent components have lower eigenvalues, representing a diminishing level of variation.

702 Table 3 presents displays the eigenvalues, the percentage of variance explained by each component, and the cumulative
703 percentage of variance.

704 **Table 3. PCA results in term of the eigenvalues, percentage of variance and cumulative percentage of variance.**

	Dim-1	Dim-2	Dim-3	Dim-4	Dim-5	Dim-6	Dim-7	Dim-8	Dim-9
Eigenvalues (λ_s) or variance	5.278	1.458	0.884	0.499	0.378	0.195	0.167	0.093	0.048
Percentage of variance	58.645	16.204	9.825	5.542	4.204	2.170	1.852	1.028	0.530
Cumulative perc. of variance	58.645	74.849	84.674	90.216	94.420	96.589	98.441	99.470	100.000

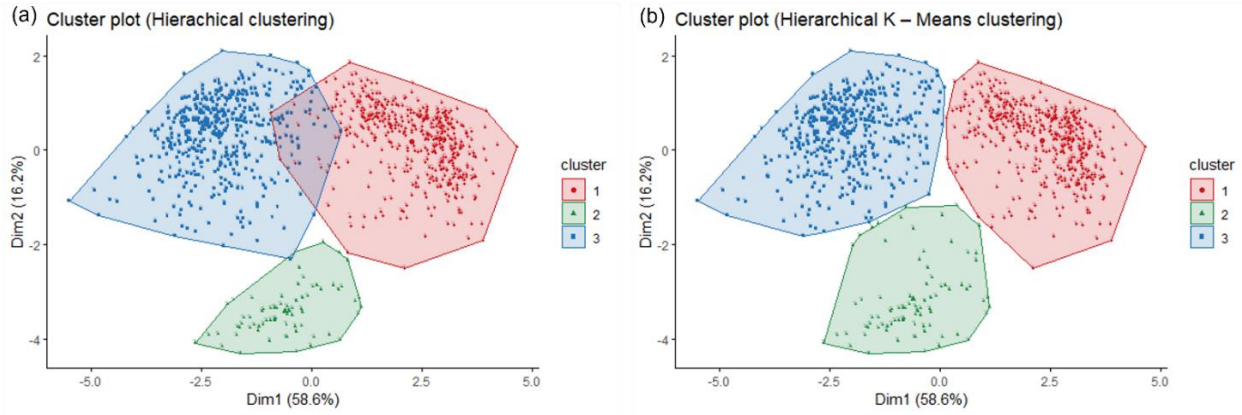
705

706 The first two principal components capture 74.85% of the total variance in the dataset. These components define a plane
707 that provides significant insights into the underlying patterns and structure of the data. Eigenvalues greater than 1 (Table
708 3) signify that the respective principal components explain more variance in the data compared to any single standardized
709 variable. ~~These principal components capture significant patterns and structures in the data, contributing more to the~~
710 ~~overall variability.~~ In contrast, eigenvalues less than 1, starting from the third principal component (Table 3) indicate that
711 the associated principal components explain less variance than individual standardized variables, suggesting they have
712 relatively less influence on the overall variability in the data. Therefore, it is probably not useful to interpret the next
713 dimensions and better focusing on the first two principal dimensions for a more meaningful analysis. It is worth
714 mentioning that the percentage of variance explained by the first principal component (58.65 %) is very close to the
715 variance explained by the hierarchical tree when is partitioned into three clusters (59.54 %).

716 The three clusters, founded using the Wards' method only, are represented in terms of solutions in the principal component
717 map (~~Figure 11~~Figure 11a). This figure shows how solutions are grouped together into three clusters when the overall
718 cloud of solutions is projected into the first two principal components. Here, cluster 1 is not very well separated from
719 cluster 3, which means that both clusters share similar solutions.

720 To enhance the distinctiveness of the cluster partitioning, the K-Means algorithm is subsequently applied. This refinement
721 step adjusts the initial partitioning obtained through Ward's method. The K-Means algorithm optimizes cluster separation
722 by iteratively recalculating the centroids for each cluster and reassigning solutions according to their proximity in
723 Euclidean space. This procedure incrementally increases the ratio of between-cluster variance to the total variance, which
724 results in the reduction of overlap and a clearer delineation of clusters. The process continues until the improvement in
725 this variance ratio does not exceed a certain threshold, thus solidifying the partitioning. The iterative optimization by the
726 K-Means algorithm is what transforms the initial, less distinct clusters arrangement (Figure 11a) into a final partitioning
727 where clusters are well-separated and more compact (Figure 11b). This refined partitioning is not only more visually
728 apparent but also statistically significant, and it is this final configuration that is retained for further analysis within the
729 paper.~~In order to have a better partitioning, the partition is improved (or "consolidated") by applying the K-Means~~
730 ~~algorithm to the initial partition (Figure 11a) founded by the Wards' method. Figure 11b shows the principal component~~
731 ~~map of the final partitioning of the solutions as result of the application of the K-means algorithm. The application of the~~
732 ~~K-Means algorithm improves the partitioning quality since the three clusters this time are very well separated from each~~
733 ~~other and are more compact. This final partitioning is therefore maintained and used for the next analysis of this paper.~~

ha fo
New



734 **Figure 11. (a). Solutions' clusters partitioning on the principal component map, using the Ward's method only. (b) Solutions'**
 735 **clusters partitioning using the Hierarchical K-Means method.**

736

737 **5.3 Further considerations on the model's parameters**

738 In Table 4, each standardized variable \hat{V}_k is presented as a vector, summarizing observations from the 1024 solutions.
 739 This forms the basis for the analysis focusing on the first two principal components, denoted as \mathbf{p}_1 and \mathbf{p}_2 .
 740 provides insights into the interpretation of the results from the perspective of the variables, focusing on the first two principal components
 741 \mathbf{p}_1 and \mathbf{p}_2 . The table displays the correlations $r_s = r(\hat{V}_k, \mathbf{p}_s)$ (where $s = 1, 2$) between the variables and these components
 742 (column 1 and 4). Additionally, the table includes the quality of the representation (qtr_s , i.e., projection) of each variable
 743 on the first two principal components (columns 2 and 5), and as well as the weight of each variable qtr_s into
 744 the construction of these components (columns 3 and 6) (Husson and Pagès (2017)). The quality of representation, $qtr_s = r_s^2$,
 745 measures the extent to which a variable is accurately projected onto a principal component. The weight of a variable,
 746 $qtr_s = \frac{r_s^2}{\lambda_s} \cdot 100\%$, quantifies the variable's relative contribution to the variance explained by the principal component, with λ_s being
 747 the eigenvalue corresponding to that component (Husson and Pagès, 2017).

748 ~~It is important to note that the variables in the Table 4 are vectors which represent the values observed across the 1024~~
 749 ~~solutions.~~

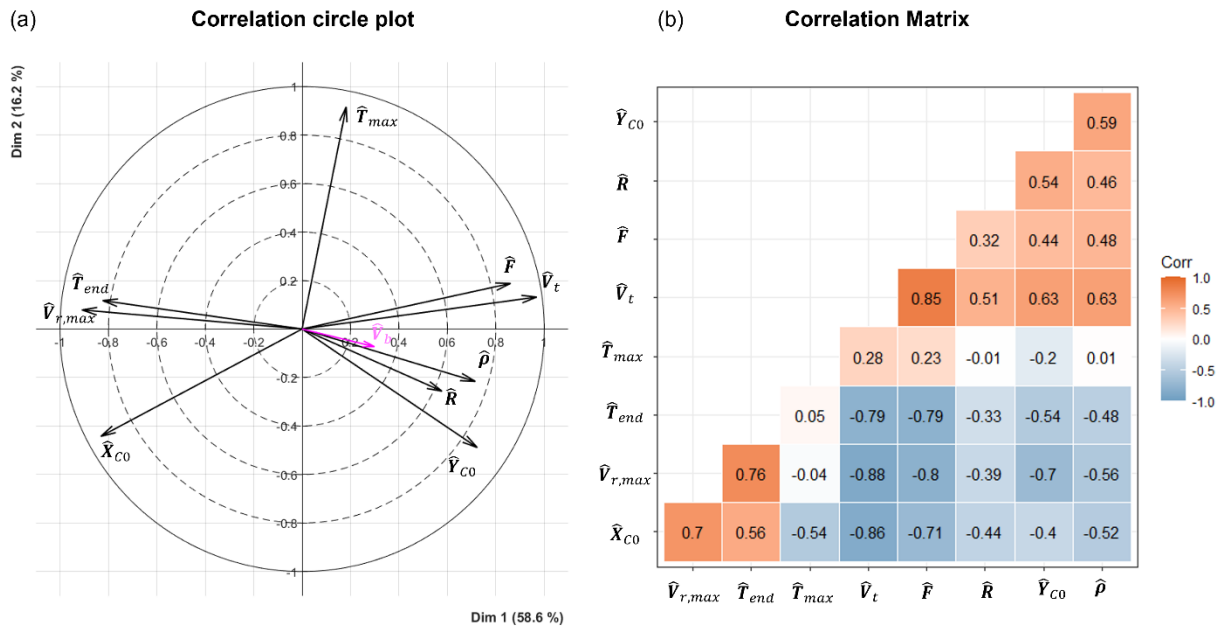
750 Table 4. Principal component analysis results for variables in terms of correlations (r), quality of representation (qtr), and contribution
 751 to the construction (qtr) relative to the first two principal components. \hat{V}_k represents the k-th standardized variable; \mathbf{p}_1 and \mathbf{p}_2 denotes
 752 the first and the second principal components, respectively.

Variables \hat{V}_k	Dim-1 $r(\hat{V}_k, \mathbf{p}_1)$	Dim-1 $qtr_1(\hat{V}_k)$	Dim-1 $qtr_1(\hat{V}_k)$	Dim-2 $r(\hat{V}_k, \mathbf{p}_2)$	Dim-2 $qtr_2(\hat{V}_k)$	Dim-2 $qtr_2(\hat{V}_k)$
\hat{X}_{CO}	-0.831	0.691	13.094	-0.443	0.196	13.441
\hat{Y}_{CO}	0.723	0.523	9.912	-0.489	0.239	16.377
\hat{R}	0.578	0.334	6.326	-0.256	0.066	4.504
$\hat{\rho}$	0.715	0.512	9.699	-0.216	0.047	3.200
$\hat{V}_{r,max}$	-0.909	0.827	15.664	0.079	0.006	0.424
\hat{T}_{max}	0.182	0.033	0.628	0.916	0.839	57.502
\hat{T}_{end}	-0.823	0.678	12.847	0.117	0.014	0.942
\hat{V}_t	0.969	0.939	17.789	0.132	0.017	1.189

\hat{F}	0.861	0.741	14.042	0.188	0.035	2.421
<i>Secondary variable</i>						
\hat{V}_b	0.299	0.089	-	-0.073	0.005	-

774

775 In Table 4, is also presents the secondary variable \hat{V}_b . The other two variables \hat{a}_t and \hat{a}_b are non-considered in
 776 the PCA due to their circular nature, which does not align well with the linear interpretation framework of principal
 777 component analysis, since their interpretation is not consistent with the principal component analysis approach. Despite
 778 \hat{V}_b not being involved in the construction of the principal components, it is still possible to evaluate the correlation and
 779 the quality of the representation of this variable using the two principal components. To facilitate the interpretation of
 780 Table 4, a correlation circle plot (Abdi and Williams, 2010) can be used to visually represent the variables. This plot
 781 represents each variable as a point in a two-dimensional space, where the coordinates of each point correspond to the
 782 correlation coefficients between the variable and the two principal components (i.e., $r(\hat{V}_k, \mathbf{p}_1), r(\hat{V}_k, \mathbf{p}_2)$). Figure 12a
 783 illustrates the correlation circle plot.



784 Figure 12. (a) Correlation circle plot. The variables in black are considered as primary variables whereas the variable in
 785 magenta is a secondary variable (b) Correlation matrix plot.

786 The plot geometrically represents variable correlations: the angles between the variables indicate the level of correlations
 787 between variables, with acute angles suggesting positive correlation and obtuse angles indicating negative correlation.
 788 This plot offers a geometric representation of the correlations among all variable pairs, making it easier to observe the
 789 grouping of positively correlated variables and the positioning of negatively correlated variables on opposite sides relative
 790 to the origin. Each variable's total contribution across all principal components equals 1. Variables fully explained by the
 791 first two components will be located on the circle's circumference (radius 1) in the correlation circle. Variables not well
 792 represented by these components will be near the center, indicating that only those near the circumference are significantly
 793 represented. The total contribution of each variable's representation across all principal components is always equal to
 794 1 (i.e., $\sum_{s=1}^K q_l t_s(V_k) = 1$). If a variable is explained by the first two components, then the sum of its contribution

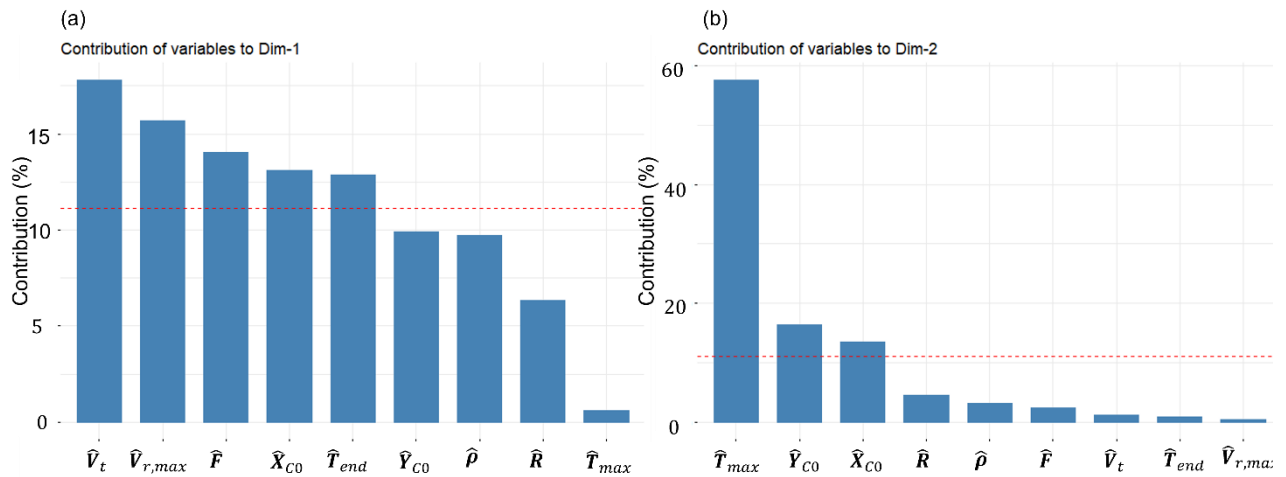
824 $\sum_{s=1}^{K=2} q_l t_s (V_{t_s})$ will be equal to 1. This implies that the variable's location on the correlation circle will exactly lie on the
 825 circumference of radius 1. Hence, a low quality variable, which is not very well represented by the first two principal
 826 components will be positioned close to the center of the circle. Therefore, only well represented variables can be
 827 interpreted from the correlation circle. Except for the variables \hat{V}_b and \hat{R} which are not very well represented by the 2
 828 first two principal components, the remaining variables are very well represented since their tip is close to the circle of
 829 radius 1. The set of variables $\{\hat{V}_t, \hat{F}, \hat{Y}_{C0}, \hat{\rho}\}$ are positively correlated, increasing together, similarly to with each other;
 830 this means that an increase in one variable is followed by an increase in the other variable. The same is true for the
 831 variables $\{\hat{V}_{r,max}, \hat{X}_{C0}, \hat{T}_{end}\}$. The variable \hat{V}_t is highly correlated with the first component-dimension (correlation of
 832 0.97). Essentially \hat{V}_t can be viewed as a representative summary of the first principal component axis. This variable could
 833 therefore summarize itself the first principal component axis. From Figure 12a it is possible to show
 834 that the variable \hat{V}_t has a strong negative correlation with the variables $\{\hat{V}_{r,max}, \hat{X}_{C0}, \hat{T}_{end}\}$. This suggests that high storm
 835 motion values V_t correspond with lower maximum radial velocities $V_{r,max}$, position closer to the station for positive values
 836 of X_{C0} , farther for negative values, and shorter downburst duration T_{end} .

837 is strongly negatively correlated with the variables $\{\hat{V}_{r,max}, \hat{X}_{C0}, \hat{T}_{end}\}$. This means for example that solutions which are
 838 characterized by high value of storm motion V_t will systematically be characterized by low values in the maximum radial
 839 velocity $V_{r,max}$, "low values" of the touch down component X_{C0} with respect to the station (which means that for lower
 840 positive values of X_{C0} , X_{C0} will be close to the station, while for lower negative values of X_{C0} , X_{C0} will be far from the
 841 station) and low values of the total duration of the downburst event T_{end} . Since \hat{V}_t is positively correlated with the
 842 variables $\{\hat{F}, \hat{Y}_{C0}, \hat{\rho}\}$, what is true for \hat{V}_t with respect to the group of variables $\{\hat{V}_{r,max}, \hat{X}_{C0}, \hat{T}_{end}\}$, will also remain true
 843 for the variables $\{\hat{F}, \hat{Y}_{C0}, \hat{\rho}\}$. Finally, from the correlation circle plot, it seems that the variable \hat{T}_{max} is not very well
 844 "linearly" correlated with the groups of variables $\{\hat{V}_{r,max}, \hat{T}_{end}, \hat{\rho}\}$ since it is nearly orthogonal with these variables. From
 845 a quantitative point of view the values of the correlation coefficients between all the pairs of variables are plotted in Figure
 846 12b. Table 4 lists each variable's contributions to the first and second principal components (columns 3 and 6
 847 respectively). Figure 13a and 13b graph these contributions in percentages, showing which variables have the most impact
 848 on these two components.

849 Table 4 shows also the values of the variable's contribution for the construction of the two principal components
 850 (columns 3 and 6 respectively). Also in this case, it is possible to plot these values to understand which variable contribute
 851 the most for building the first two principal axes. Figure 13a and Figure 13b show respectively the contribution of the
 852 variables expressed in percentage for the reconstruction of the first two principal components.

ha fo
New

ha fo
New



881 **Figure 13. (a) Contribution of the variables in the reconstruction of the first principal component (Dim-1). (b) Contribution**
 882 **of the variables in the reconstruction of the second principal component (Dim-2). Variables are sorted from the strongest to**
 883 **the weakest. The red dashed line indicates the expected average contribution.**

884 The graph shows a red dashed line indicating the average expected variable contribution at 11.11 %, based on 9 variables.
 885 displays a red dashed line representing the expected average contribution. If the contribution of variables were evenly
 886 distributed, the expected value would be calculated as 1 divided by the number of variables K , which in this case is 9.
 887 This would result in an expected average contribution of 11.11%. Variables with contributions over 11.11% significantly
 888 construct a principal component. For the first component, $\{\hat{V}_t, \hat{V}_{r,max}, \hat{F}, \hat{X}_{CO}, \hat{T}_{end}\}$ are key contributors. For the second,
 889 $\{\hat{T}_{max}, \hat{Y}_{CO}, \hat{X}_{CO}\}$ are most influential. The leading contributors for both components combined, ranked by importance in
 890 building the first two principal components are $\{\hat{V}_t, \hat{X}_{CO}, \hat{T}_{max}, \hat{V}_{r,max}, \hat{F}, \hat{Y}_{CO}\}$. The remaining variables $\{\hat{T}_{end}, \hat{\rho}, \hat{R}\}$ fell
 891 below the average contribution of 11.11 %. It is worth mentioning that the categorization of variables from stronger to
 892 weaker is not universal since the partitioning might depend on the downburst case under investigation.

893 For a given component, a variable with a contribution larger than this cutoff could be considered as important in
 894 contributing to the construction of the component. Therefore, the set of variables $\{\hat{V}_t, \hat{V}_{r,max}, \hat{F}, \hat{X}_{CO}, \hat{T}_{end}\}$ contribute the
 895 most to the construction of the first principal component (Dim 1), while the set of variables $\{\hat{T}_{max}, \hat{Y}_{CO}, \hat{X}_{CO}\}$ contributes
 896 the most for the construction of the second principal component (Dim 2). Since the contribution can be added, the set of
 897 variables that contributes the most for the construction of Dim 1 and 2 are given by the set of variables
 898 $\{\hat{V}_t, \hat{X}_{CO}, \hat{T}_{max}, \hat{V}_{r,max}, \hat{F}, \hat{Y}_{CO}\}$ which are ordered from the strongest to the weakest. The remaining variables $\{\hat{T}_{end}, \hat{\rho}, \hat{R}\}$
 899 have a contribution which is lower than the threshold 11.11 %. It is important to observe the partitioning in strongest
 900 variables and weakest ones does not represent necessarily a general case, since the partition might depend on the
 901 downburst case under study.

902 5.4 Physical description of the solutions corresponding to clusters 1-3

903 Once the partitioning of the solutions of the optimization problems in three cluster is completed, it is important to have a
 904 closer look at them and describe common features of solutions which belong to the same cluster. From the partition
 905 analysis, it is found that cluster 1 is made up of 481 solutions, cluster 2 of 85 and cluster 3 of 458 solutions. Table 5
 906 summarizes a few key statistics related to the three clusters. This table includes primary and secondary (i.e., not used
 907 for clustering) variables, which are no longer standardized to investigate their physical meaning.

ha fo
New

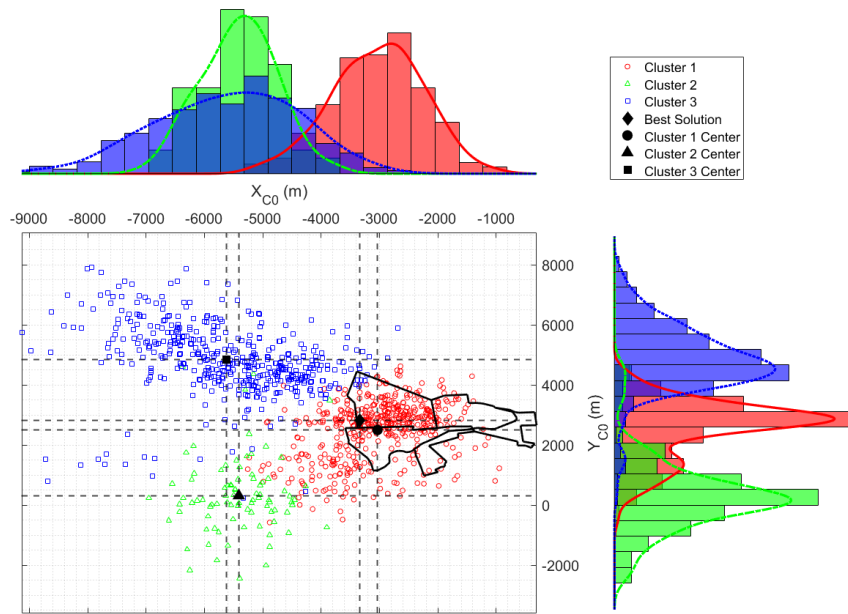
919 **Table 5. Description of the partition by the mean and standard deviation of all the variables.**

Variables V_k	Overall Mean	Overall Std	Cluster 1 Mean	Cluster 1 Std	Cluster 2 Mean	Cluster 2 Std	Cluster 3 Mean	Cluster 3 Std
V_t (m/s)	6.025	3.371	2.811	1.042	6.527	1.407	9.307	1.492
X_{C0} (m)	-4386.350	1613.337	-3034.079	789.682	-5410.461	629.282	-5616.465	1209.346
T_{max} (min)	6.954	2.517	5.860	1.172	13.336	1.910	6.919	1.797
$V_{r,max}$ (m/s)	24.293	5.356	28.639	1.465	28.182	1.793	19.006	3.266
F (-)	0.893	0.080	0.823	0.058	0.919	0.043	0.961	0.021
Y_{C0} (m)	3363.669	1809.316	2499.896	975.450	313.553	1257.946	4836.890	1160.613
T_{end} (min)	26.035	3.167	28.269	1.895	27.622	2.295	23.394	2.235
ρ (-)	2.189	0.108	2.126	0.104	2.134	0.100	2.265	0.050
R (m)	1334.478	102.519	1289.518	124.661	1301.969	90.475	1387.728	23.115
Secondary variables								
α_t (deg)	290.383	0.480	276.439	0.416	253.518	0.217	310.868	0.229
V_b (m/s)	6.811	0.670	6.648	0.774	6.705	0.768	7.002	0.449
α_b (deg)	268.218	0.118	264.854	0.138	273.055	0.074	270.827	0.055

920

921 In columns 2-3, the overall mean, and the overall standard deviation (std) are calculated with respect to each variable
 922 (primary and secondary). In the other columns, the same calculation was repeated taking into consideration the three
 923 clusters. Mean and the std of the secondary variables α_t and α_b have been calculated using circular statistics (Rao and
 924 Sengupta, 2001). To start clarifying the characteristics of the different clusters, [Figure 14](#) ~~Figure 14~~ shows the scatter plot
 925 and distribution of the touchdown components (X_{C0} , Y_{C0}) for all the solutions, partitioned into three clusters. In this figure
 926 it is shown the center (namely the mean) of each cluster and the location of the touchdown position of the best overall
 927 solution. The figure shows also with a black line the position of the city of Sânnicolau Mare. Also, on the left and on the
 928 top of this figure is possible to show the histograms of the variable (X_{C0} , Y_{C0}) relative to each cluster.

ha fo
New



946 **Figure 14. Scatter plot and histogram density distribution for the variables (X_{C0}, Y_{C0}). The dark black line shows the**
 947 **contours of the city Sânnicolau Mare.**

948
 949 The three clusters appear well separated in terms of touchdown position (X_{C0}, Y_{C0}). Since it is very unlikely that the
 950 cluster means coincide with one of the solutions present in the data set, let's define as "cluster solution", the solution
 951 which is the closest to the mean of the cluster across all variables. Accordingly, the cluster solutions, reported in Table
 952 6Table-6, will be used to interpret the average features of each cluster. The first row of this table is dedicated to the best
 953 solution founded by the optimization algorithm (i.e., the one that have the lowest objective function F among all the
 954 solutions); the best solution belongs to Cluster 1.

955 **Table 6. Overall best solution and clusters representative solutions.**

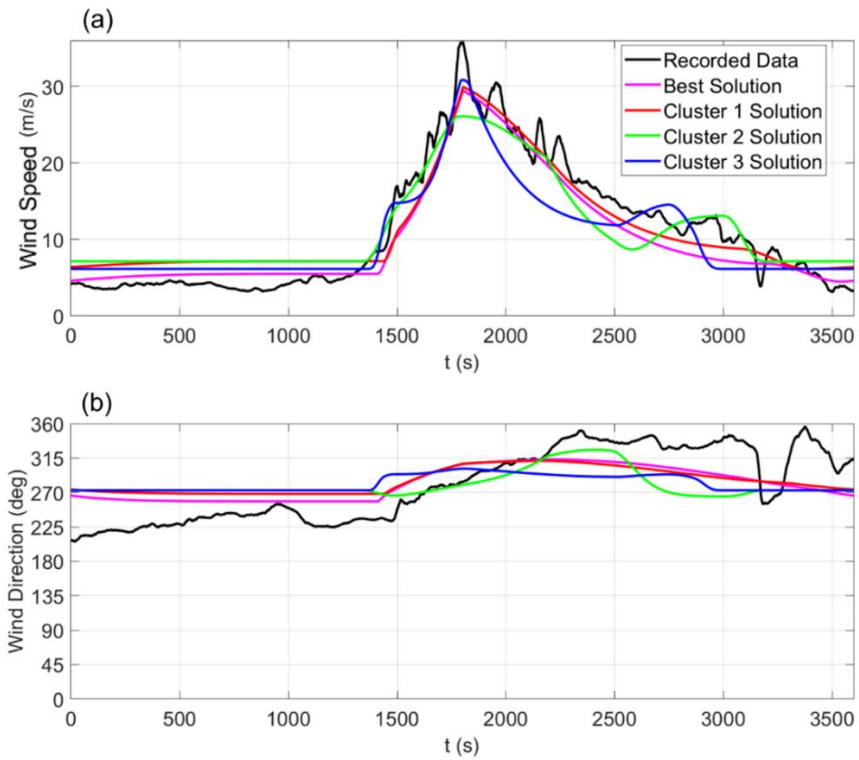
956

Solutions	V_t (m/s)	X_{C0} (m)	T_{max} (min)	$V_{r,max}$ (m/s)	F (-)	Y_{C0} (m)	T_{end} (min)	ρ (-)	R (m)	α_t (deg)	V_b (m/s)	α_b (deg)
Best solution	2.76	-3339.53	6.50	29.80	0.73	2826.55	29.89	2.15	1381.38	271.74	5.49	58.35
Cluster 1	2.51	-2944.15	6.05	29.54	0.81	2769.36	27.23	2.09	1287.53	278.25	7.15	268.19
Cluster 2	6.14	-5105.66	14.05	27.07	0.91	383.39	28.18	2.14	1295.33	255.36	7.13	272.82
Cluster 3	9.25	-5930.81	7.15	17.36	0.97	4575.50	22.95	2.27	1392.86	307.61	6.15	272.71

957
 958 Figure 15Figure-15 shows the time histories produced by the best solution and the three cluster solutions, in terms of
 959 wind velocity (Figure 15Figure-15a) and direction (Figure 15Figure-15b), compared with the moving averaged recorded
 960 data. The figure provides a qualitative representation of the goodness of fit between the simulations and the recorded data.
 961 The goodness of fit is quantitatively measured by the objective function F . The simulations produced from the best
 962 solution and the Cluster 1 solution fit the data better than Cluster 2 and 3. This is quite obvious since the best solution

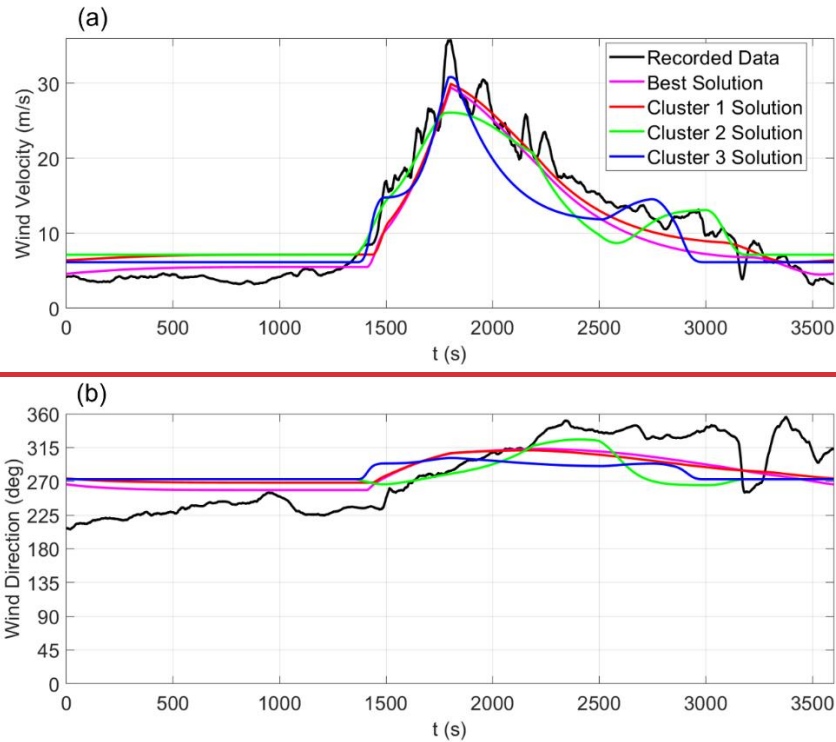
967 have the lowest objective function F and belongs to Cluster 1, whereas Cluster 2 and Cluster 3 solutions have slightly
968 higher objective function values F (refer to column 5 in [Table 6-Table 6](#)).

ha fo
New



969

970

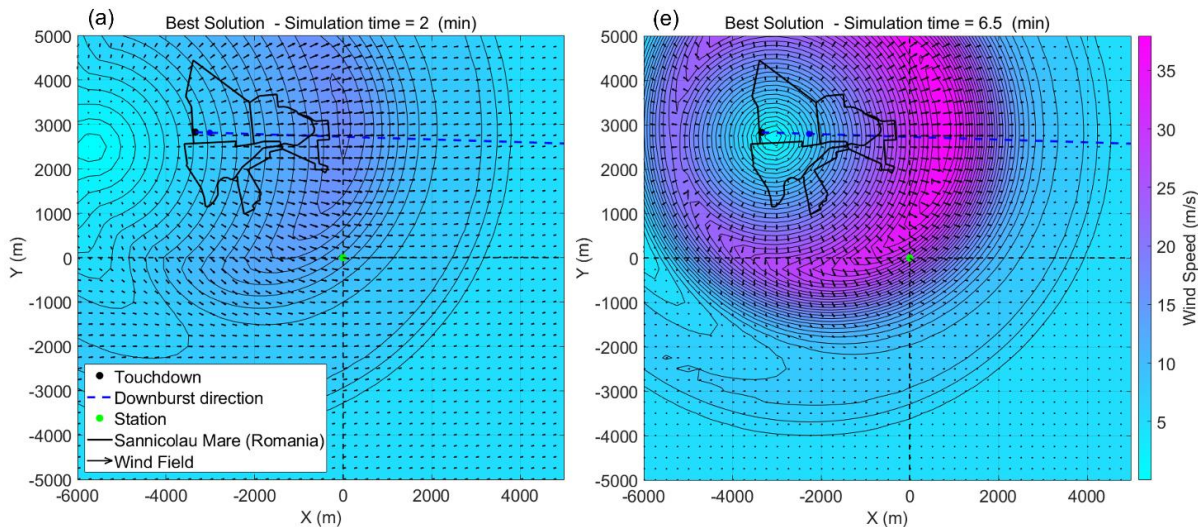


981

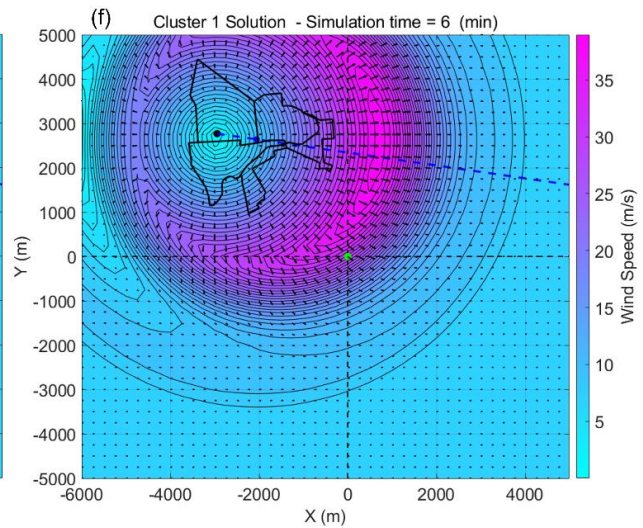
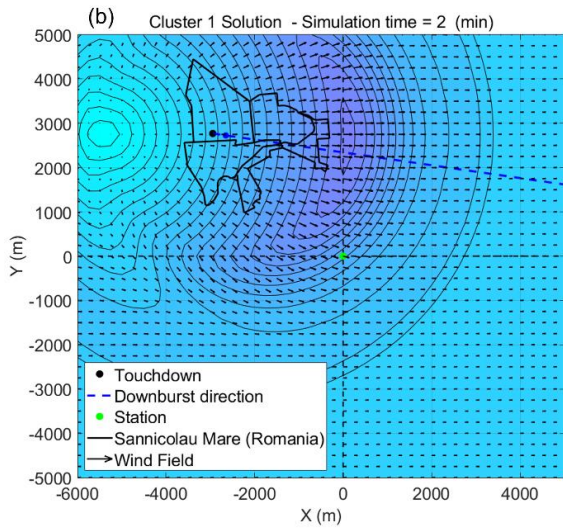
982 **Figure 15. Comparison among the moving averaged wind speed (a) and direction (b) obtained from the measurements of the**
 983 **Sănnicolau Mare downburst, along with the best solution and the three cluster solutions.**

984 In order to better understand the nature of the different solutions relative to each cluster, for each solution present in [Table](#)
 985 [6Table-6](#), the downburst 2D wind velocity is evaluated at the same height of the anemometric station (i.e., at 50 m AGL).
 986 The left panels of [Figure 16Figure-16](#) (from (a) to (d)) show for each of the 4 solutions the wind field reconstruction
 987 during the intensification stage of the downburst, while the right panels (from (e) to (h)) describes the stage of maximum
 988 intensity. Note that the time of maximum intensity is different for each cluster according to the corresponding value of
 989 T_{max} reported in column 3 of [Table 6Table-6](#).

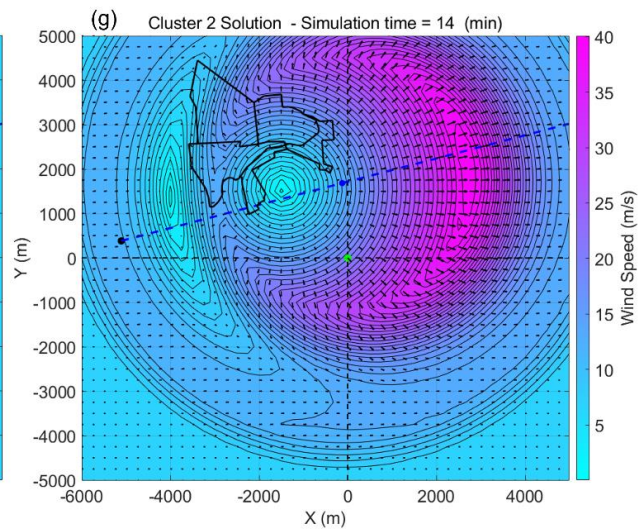
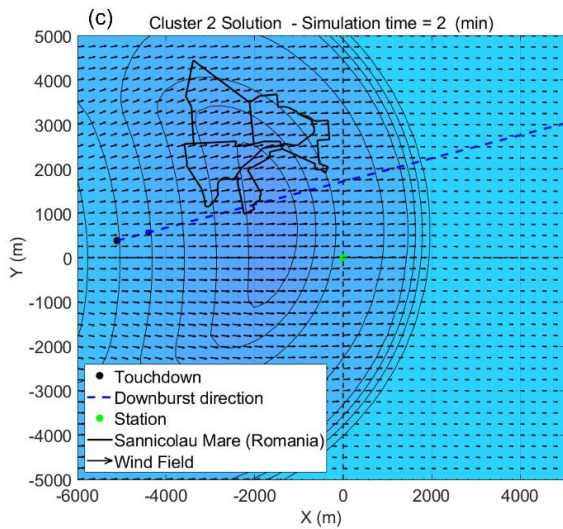
ha fo
New
ha fo
New
ha fo
New



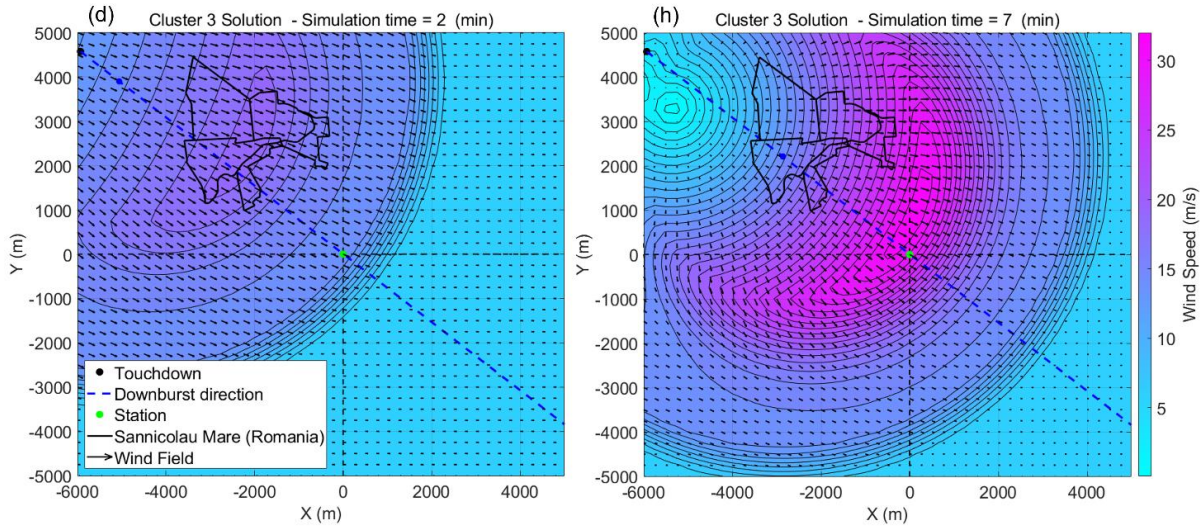
990



991



992



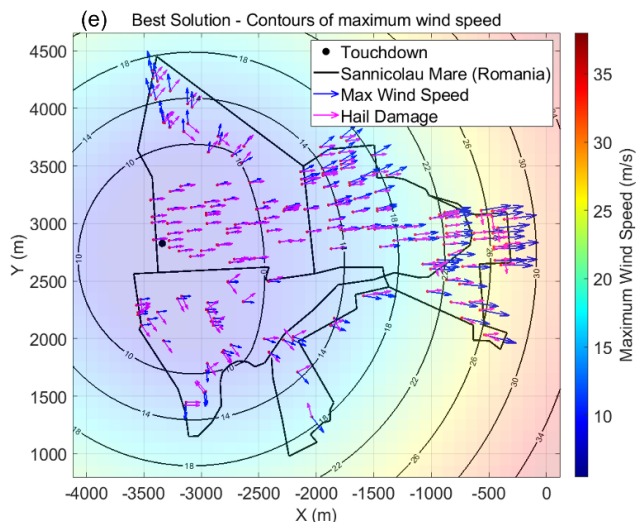
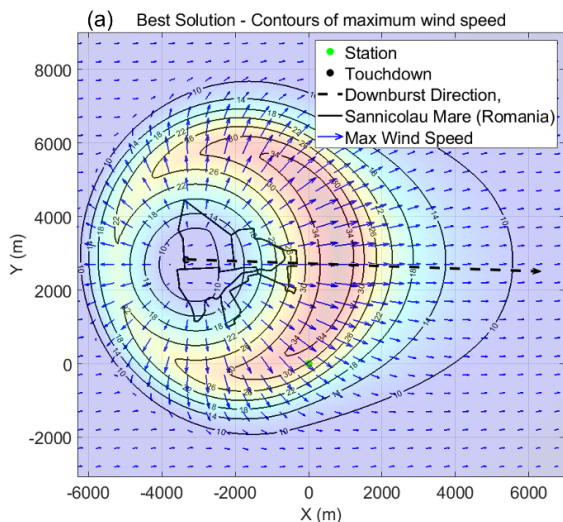
993

994 **Figure 16. 2D wind field reconstruction at 50 m AGL. From (a) to (d), the best solution, Cluster 1, 2 and 3 solutions are depicted**
 995 **at the intensification stage of the downburst. From (e) to (h), the best solution, Cluster 1, 2 and 3 solutions are depicted at the**
 996 **maximum intensification stage of the downburst.**

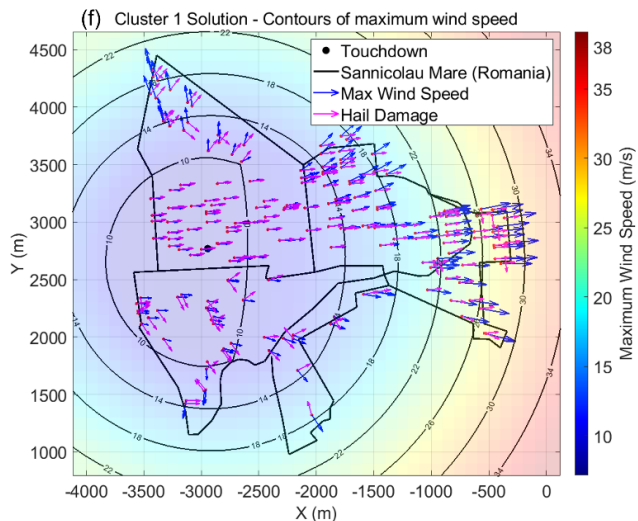
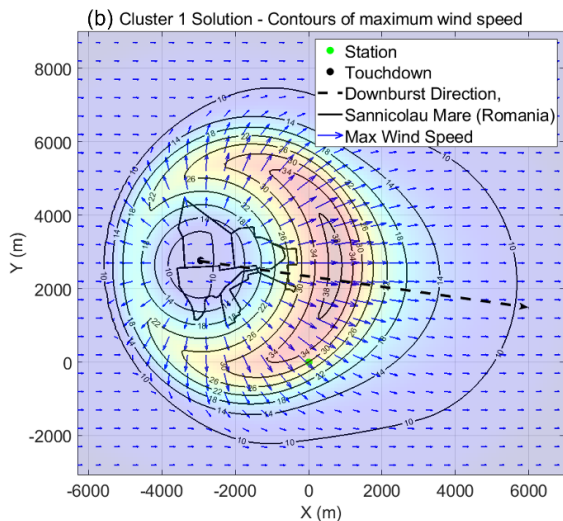
997 Cluster 1 touches down very close to the city center and moves slowly eastward, it is characterized by a low value of the
 998 downburst translation velocity V_t , with mean value 2.8 m/s against the overall mean among all clusters which is 6.0 m/s.
 999 In addition, it has maximum radial velocity $V_{r,max}$ higher and overall duration of the downburst event T_{end} longer with
 1000 respect to the mean values of the other two clusters. The solutions belonging to Cluster 2 touch down around 2 km
 1001 southwest of the city, they propagate northeastward with higher translation velocities compared to Cluster 1 and the
 1002 longest intensification periods T_{max} overall. The solutions in Cluster 3 touch down about 3 km northwest of the city, they
 1003 move southeastward with the highest values of downburst translation velocity V_t but they are the lowest-lasting as the
 1004 duration of the downburst event T_{end} is on average 23.4 min while the overall mean is 26.0 min. They also have the
 1005 lowest values of maximum radial velocity $V_{r,max}$ which compensate the high translation velocities. According to these
 1006 descriptions, it is clear that in the solution's space of the model three different solutions exist that can describe similarly
 1007 the time-series measured at TM_424. The existence of different plausible solutions means that the problem of finding the
 1008 downburst wind field time-space evolution using a single time-series is an underdetermined problem.

1009 The Sannicolau Mare downburst had a strong impact, causing hail damage to numerous buildings in the town. A damage
 1010 survey was conducted to assess the affected areas and identify buildings that experienced hail damage during the event.
 1011 To estimate the extent of the damage, the simulated wind field generated by the analytical model was utilized. By
 1012 analyzing the wind speeds at various locations, the "footprint" of the simulated damage was determined. This footprint
 1013 represents the maximum wind speed recorded at different places during the downburst, providing valuable information
 1014 on the areas most affected by the event. The left panels of Figure 17, labeled from (a) to (d), depict the complete footprint
 1015 of the downburst potential damage area for the best solution and the three cluster solutions. In contrast, the right panels,
 1016 labeled from (e) to (h), provide a closer view of the footprints overlaying the simulated maximum wind velocity vectors
 1017 (indicated by blue arrows) onto the locations of hail damage. The hail damage is represented by vectors pointing
 1018 orthogonally to the damaged facades (represented by pink arrows). The comparison between the facades damage, which
 1019 is related to the trajectory of hail transported by the strong downburst-related outflow, and the simulated maximum

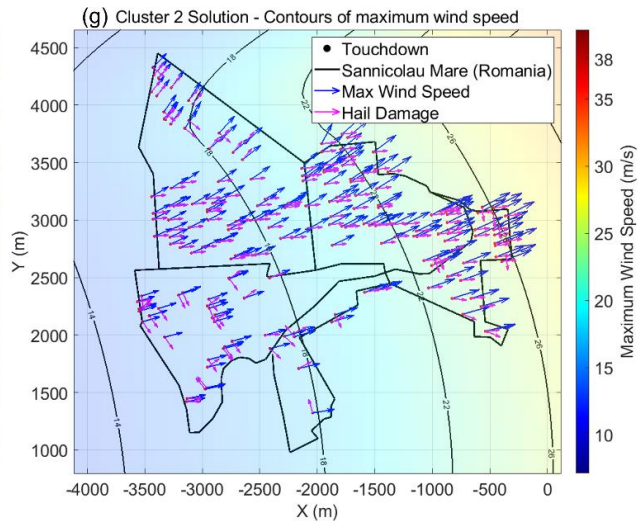
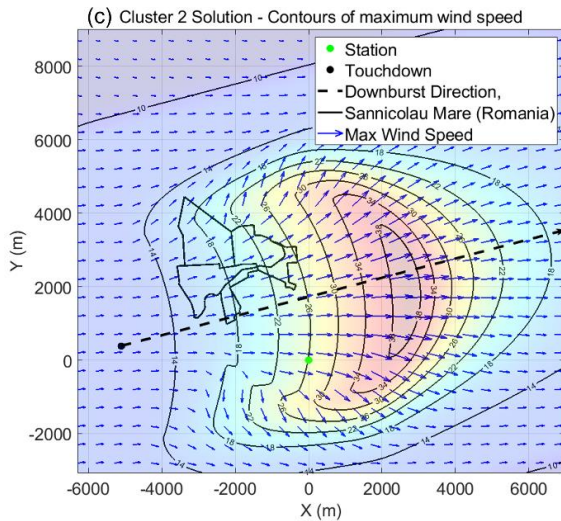
1020 velocity reveals interesting findings. Specifically, the best solution and Cluster 1 solutions exhibit the strongest alignment
 1021 between the maximum wind velocity vectors and hail damage vectors, particularly in the central part of the city and along
 1022 the path of the downburst. In contrast, Cluster 2 and Cluster 3 demonstrate a consistent deviation of the maximum velocity,
 1023 with Cluster 2 deviating northward and Cluster 3 deviating southward, relative to the hail trajectories. This observation
 1024 suggests that the actual downburst event likely followed a pattern more closely resembling Cluster 1 rather than the other
 1025 two potential solutions.



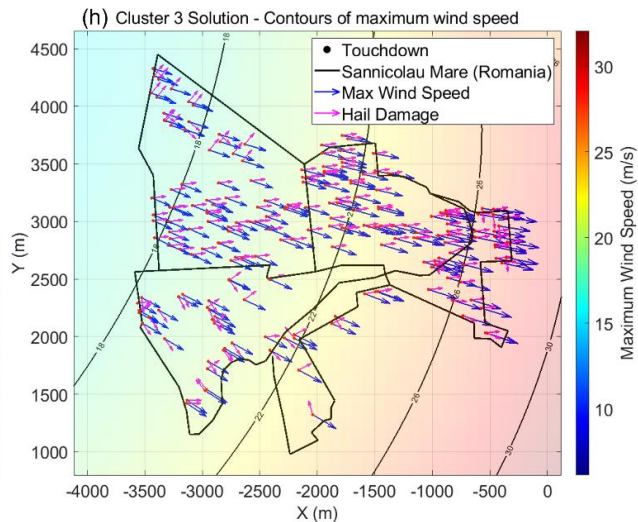
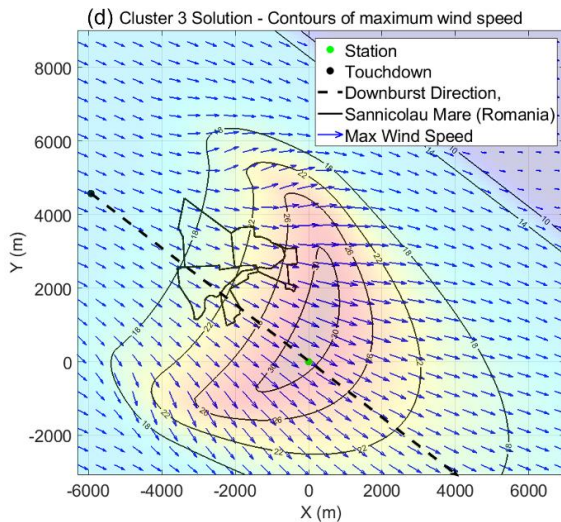
1026



1027



1028



1029

1030 **Figure 17. Simulated footprints of the downburst that occurred in Sannicolau Mare. Panels from (a) to (d) representing the**
 1031 **footprints for the best solution, Cluster 1, Cluster 2, and Cluster 3 respectively. Panels from (e) to (h), representing**
 1032 **comparison between hail damage and maximum simulated wind speed for the best solution, Cluster 1, Cluster 2, and Cluster**
 1033 **3 respectively.**

1034 These observations lead to the conclusion that the optimal (best) solution, which minimizes the objective function F , is
 1035 the most reliable among all possible solutions. In the current study, this has been achieved through a comprehensive
 1036 approach involving numerous simulations, specifically tailored for cases where only anemometric data is available,
 1037 despite having access to additional data types like the Radar images. This choice was driven by the higher likelihood and
 1038 frequency of availability of anemometric data in practical scenarios, thus providing a more universally applicable context
 1039 for the analytical downburst model. The methodology involved conducting a large number of simulations to thoroughly
 1040 explore the solution space, given the data-limited scenario. Consequently, this approach enabled the extraction of
 1041 kinematic and geometric parameters of the downburst outflow wind field exclusively from anemometric data.

1042 However, it is important to acknowledge that in scenarios where additional data types such as Radar or Lidar or other
1043 sensors are available, the approach to reconstructing the downburst wind field would differ significantly. In such
1044 situations, the availability of more diverse data allows for a more constrained and targeted reconstruction process. By
1045 integrating specific parameters ~~form~~from these additional data sources, like storm speed and direction and ABL wind
1046 speed and direction, the solution space can be narrowed down more effectively, potentially reducing the number of
1047 simulations needed and enhancing the precision of the model.

1048 ~~This implies that the reconstruction of the downburst wind field should be based on a large number of simulations to~~
1049 ~~ensure that the optimal solution is obtained. By conducting numerous simulations, the likelihood of obtaining the most~~
1050 ~~accurate representation of the downburst event is maximized leading to a more accurate reconstruction of the event.~~

1051

1052

1053 **6 Conclusions**

1054 This study focuses on the analysis of solutions obtained by combining an analytical model (Xhelaj et al., 2020) with a
1055 global metaheuristic optimization algorithm for the reconstruction of the wind field generated during the Sânnicolau Mare
1056 downburst event in Romania on June 25, 2021. The analytical model and optimization algorithm are coupled using the
1057 Teaching Learning Optimization Algorithm (TLBO) to estimate the kinematic parameters of the downburst outflow. The
1058 procedure for this coupling and parameter estimation is described in detail in the study by Xhelaj et al. (2022). Therefore,
1059 the objective was to analyse the differences among the solutions provided by the optimization algorithm and to assess
1060 their physical validity as alternatives to the optimal solution. In the presence of multiple physically sounding solutions, it
1061 has been demonstrated that additional data describing the downburst thunderstorm event is necessary to determine which
1062 solution best represents reality. To support the analysis a comprehensive damage survey was conducted in collaboration
1063 with the University of Genoa (Italy) and the University of Bucharest (Romania) to assess the extent and location of hail
1064 damage on buildings in the affected area. This survey, along with the wind speed and direction signals recorded during
1065 the downburst event by a telecommunication tower located approximately 1 km from the city, significantly enhances the
1066 information available for the reconstruction and simulation of the downburst using the optimization procedure. The
1067 analysis of the solutions generated by the optimization algorithm involves multivariate data analysis (MDA) techniques,
1068 specifically agglomerative hierarchical clustering coupled with the ~~K-means~~Means algorithm (AHK-MC) and principal
1069 component analysis (PCA). The AHK-MC is used for classifying the solutions into different clusters based on their
1070 features, while PCA is employed to determine the importance of the variables in the analytical model for the downburst
1071 event reconstruction.

1072 The application of AHK-MC resulted in the identification of three main clusters, each with distinct characteristics, among
1073 the 1024 solutions.

- 1074 • Solutions belonging to Cluster 1 are characterized by a slow storm motion, small touch down distance from the
1075 city of Sânnicolau Mare and by long duration of the downburst event. The best overall solution belongs to Cluster
1076 1.
- 1077 • Solutions belonging to Cluster 2 are characterized by a moderate storm motion and moderate distance of the
1078 touch-down from the town of Sânnicolau Mare. These solutions are also characterized by high duration of the
1079 intensification period of the downburst event.

1080 • Solutions belonging to Cluster 3 are characterized by a high storm motion and high distance of the touch-down
1081 from Sânnicolau Mare. They are also characterized by low duration of the downburst event and low values of
1082 the maximum radial velocity.

1083 The result of the MDA allows also to establish at least for the case under consideration that the set of variables
1084 $\{V_t, X_{C0}, T_{max}, V_{rmax}, F, Y_{C0}\}$ which are ordered from the strongest to the weakest are the more important for the
1085 reconstruction/simulation of the downburst event. The remaining variables $\{T_{end}, \rho, R\}$ have a lower contribution. It is
1086 important to observe the partitioning in strongest variables and weakest ones does not represent a general case, since the
1087 partition depends on the downburst case under study.

1088 Finally, the comparison between the facades damage, which are related to the trajectory of hails transported by the strong
1089 downburst-related outflow and the simulated maximum velocity shows that the best solution and Cluster 1 solutions seem
1090 to have a “good” overlapping between maximum wind velocity vectors and hail damage vectors. Considering the solutions
1091 of Cluster 2 and 3, it seems that the match between maximum wind velocity vectors gradually decreases, with the worst
1092 case represented by Cluster 3 solutions. These observations allow to conclude that the optimal solution, that is, the one
1093 that minimizes the objective function F , is the best with respect to the other three cluster solutions, also from the point of
1094 view of the damage analysis. As a result, for the specific case being examined, relying on the best overall solution provided
1095 by the optimization algorithm appears to yield promising results for reconstructing the downburst wind field. Obviously,
1096 an analysis of this type, conducted on several downburst events, will be able to better confirm this statement.

1097 **Author contributions**

1098 This paper is based on the Ph.D. thesis of Andi Xhelaj, under the guidance of Prof. Giovanni Solari and Prof. Massimiliano
1099 Burlando. Andi Xhelaj played a crucial role in conceptualizing the study, developing the methodology, organizing the
1100 data, conducting data analysis, and preparing the manuscripts and figures. The study was supervised by Prof.
1101 Massimiliano Burlando, who provided guidance and conducted internal review process.

1102 **Declaration of competing interest**

1103 The authors affirm that they have no known financial conflicts of interest or personal relationships that could have
1104 influenced the findings presented in this paper.

1105 **Acknowledgments**

1106 The authors would like to acknowledge the valuable contributions of I. Calotescu, X. Li, M.T. Mengistu, and M.P. Repetto
1107 for providing the time histories of the recorded data and the hail damage map from the survey of the Thunderstorm event
1108 in Sânnicolau Mare, Romania, on 25 June 2021. The monitoring system and damage survey were carried out as part of
1109 a research collaboration between the University of Genoa (UniGe) and the Technical University of Civil Engineering
1110 Bucharest (UTCB), funded by the European Research Council (ERC) under the European Union's Horizon 2020 research
1111 and innovation program (Grant Agreement No. 741273) for the Project THUNDERR - Detection, simulation, modeling,
1112 and loading of thunderstorm outflows to design wind-safer and cost-efficient structures, supported by an Advanced Grant
1113 (AdG) 2016. As the corresponding author is not a native English speaker, he utilized the OpenAI's GPT-4 model as an
1114 editing tool during the creation of this paper to review and amend grammatical and spelling mistakes and to ensure
1115 linguistic consistency and coherence throughout this paper.

1116

1117 **References**

1118

- 1119 1. Abd-Elaal, E.S., Mills, J.E., Ma, X., 2013. A coupled parametric-CFD study for determining ages of downbursts
1120 through investigation of different field parameters. *J. Wind Eng. Ind. Aerod.* 123, 30–42.
- 1121 2. Abdi, H., and Williams, L., J.: Principal component analysis. *Wiley Interdisciplinary Reviews: Computational*
1122 *Statistics* 2(4):433 – 459, 2010.
- 1123 3. Amato, F., Guignard, F., Robert, S. Kanevski, M.: A novel framework for spatio-temporal prediction of
1124 environmental data using deep learning. *Sci Rep* 10, 22243, doi:10.1038/s41598-020-79148-7_2020.
- 1125 4. Bjerknes, J., Solberg, H.: Life cycle of cyclones and polar front theory of atmospheric circulation. *Geophysiks*
1126 *Publikationer* 3, 3-18, 1922.
- 1127 5. Bogensperger, A., Fabel, Y. A practical approach to cluster validation in the energy sector. *Energy Inform* 4 (Suppl
1128 3), 18 (2021). <https://doi.org/10.1186/s42162-021-00177-1>.
- 1129 6. Burlando, M., Antonelli M., Ratto, C., F.: Mesoscale wind climate analysis: identification of anemological regions
1130 and wind regimes. *Int. J. Climatol.* 28(5), 629–641. DOI: 10.1002/joc.1561 – ISSN 1097-0088, 2008.
- 1131 7. Burlando, M.: The synoptic-scale surface wind climate regimes of the Mediterranean Sea according to the cluster
1132 analysis of ERA-40 wind fields. *Theor. Appl. Climatol.* 96(1), 69-83. DOI: 10.1007/s00704-008-0033-5 – ISSN
1133 0177-798X – eISSN 1434-4483, 2009.
- 1134 8. Burlando, M., Romanic, D., Solari, G., Hangan, H., Zhang, S.: Field data analysis and weather scenario of a
1135 downburst event in Livorno, Italy on 1 October 2012. *Mon. Weather Rev.* 145, 3507-3527, 2017.
- 1136 9. Calotescu, I., Bîtcă D., Repetto, M., P.: Full-scale behaviour of a telecommunication lattice tower under wind
1137 loading. *Lightweight Structures in Civil Engineering, XXVII LSCE Łódź, 2nd – 3rd of December 2021, Szafran J.*
1138 *and Kaminski M, Eds. p. 15-18, 2021.*
- 1139 10. Calotescu, I., Repetto, M., P.: Wind and structural monitoring system for a Telecommunication lattice tower. 14th
1140 *Americas Conference on Wind Engineering, May 17-19, 2022, Lubbock, TX, 2022.*
- 1141 11. Calotescu, I., Bîtcă, D., Repetto, M. P.: Full-scale monitoring of a telecommunication lattice tower under synoptic
1142 and thunderstorm winds. *J Wind Eng. Ind. Aerodyn.* (submitted), 2023.
- 1143 12. Calotescu, I., Li, X., Mengistu, M.T., Repetto, M., P.: Post-event Survey and Damage Analysis of An Intense
1144 Thunderstorm in Sannicolau Mare, Romania. 14th Americas Conference on Wind Engineering, May 17-19, 2022,
1145 Lubbock, TX, 2022.
- 1146 13. Calotescu, I., Li, X., Mengistu, M.T., Repetto, M., P.: Thunderstorm – induced damage to built environment: A field
1147 measurement and post-event survey. *J Wind Eng. Ind. Aerodyn.* (submitted), 2023.
- 1148 14. Chay, M.T., Albermani, F., Wilson, B., 2006. Numerical and analytical simulation of downburst wind loads. *Eng.*
1149 *Struct.* 28, 240–254.
- 1150 15. Davenport, A., G.: The application of statistical concepts to the wind loading of structures. *P. I. Civ. Eng.* 19, 449-
1151 472., 1961.
- 1152 16. Fujita, T., T.: Manual of downburst identification for project Nimrod. *Satellite and Mesometeorology Research Paper*
1153 156, Dept. of Geophysical Sciences, University of Chicago, 104 pp, 1978.
- 1154 17. Fujita, T., T.: Downburst: Microburst and Macrobust. *Univ. Chic. Press II*, p. 122, 1985.
- 1155 18. Glauert, M.B., 1956. The wall jet. *J. Fluid Mech.* 1, 625–643.
- 1156 19. Hartigan, J., A.: *Clustering Algorithms.* Wiley, New York, 1975.

- 1157 20. Hartigan, J., A. and Wong, M., A.: A K-means clustering algorithm. *Applied Statistics* 28, 100–108, 1979.
- 1158 21. Hjelmfelt, M.R., 1988. Structure and life cycle of microburst outflows observed in Colorado. *J. Appl. Meteorol.* 27,
1159 900–927 (August).
- 1160 22. Hjelmfelt, M.R.: Microburst and Macrobust: windstorms and blowdowns. In: Johnson, E.A., Miyanishi, K., (Eds.),
1161 *Plant Disturbance Ecology*. Academic Press, Amsterdam, pp. 59-102, 2007.
- 1162 23. Holmes, J.D., Oliver, S.E., 2000. An empirical model of a downburst. *Eng. Struct.* 22, 1167–1172.
- 1163 24. Husson, F., Lê, S., & Pagès, J.: *Exploratory Multivariate Analysis by Example Using R* (2nd edition). CRC Press,
1164 2017.
- 1165 25. Ivan, M., 1986. A ring-vortex downburst model for flight simulations. *J. Aircraft* 23 (3), 232–236.
- 1166 26. Jiang, Y., Cooley, D., Wehner, M., F.: Principal Component Analysis for Extremes and Application to U.S.
1167 Precipitation. *Journal of Climate*, Volume 33, 15, 2020.
- 1168 27. Kassambara, A.: *Practical Guide to Principal Component Methods in R (Multivariate Analysis Book 2)* (1st edition).
1169 STHDA. ASIN: B0754LHRMV, 2017.
- 1170 28. Kaufman, L. and Rousseeuw, P.: *Finding Groups in Data. An Introduction to Cluster Analysis*, Wiley & Sons, New
1171 York, 1990.
- 1172 29. Le, T.H., Caracoglia, L., 2017. Computer-based model for the transient dynamics of tall building during digitally
1173 simulated Andrews AFB thunderstorm. *Comput. Struct.* 193, 44–72.
- 1174 30. Letchford, C.W., Mans, C., Chay, M.T.: Thunderstorms – their importance in wind engineering (a case for the next
1175 generation wind tunnel). *J. Wind Eng. Ind. Aerodyn.*, 90, 1415-1433, 2002.
- 1176 31. MacQueen, J.: Some methods for classification and analysis of multivariate observations. In *Proceedings of the Fifth*
1177 *Berkeley Symposium on Mathematical Statistics and Probability*, eds L. M. Le Cam & J. Neyman, 1, pp. 281–297,
1178 1967.
- 1179 32. Markowski, P., & Richardson, Y.: *Mesoscale Meteorology in Midlatitudes*. Wiley-Blackwell, 2010. ISBN: 978-
1180 0470742136.
- 1181 33. McCarthy, J., Wilson, J.W., Fujita, T.T., The Joint Airport Weather Studies Project, 1982. *Bulletin of the American*
1182 *Meteorological Society* 63, 15–22.
- 1183 34. Oseguera, R.M., Bowles, R.L., 1988. A simple analytic 3-dimensional downburst model based on boundary layer
1184 stagnation flow. *NASA Tech. Memo.* 100632.
- 1185 35. Parker, M. D., Johnson, R. H., 2004: Structures and dynamics of quasi-2D mesoscale convective systems. *J. Atmos.*
1186 *Sci.*, 61, 545–567.
- 1187 36. Proctor, F.H., 1987a. The terminal area simulation system - Part I: theoretical formulation. *NASA Contractor Report*
1188 4046.
- 1189 37. Proctor, F.H., 1987b. The terminal area simulation system - Part II: verification cases. *NASA Contractor Report*
1190 4047.
- 1191 38. Rao, S., J., and Sengupta, A.: *Topics in Circular Statistics*. World Scientific, 2001.
- 1192 39. Rao, R.V., Savsani, V.J. and Vakharia, D.P.: Teaching–learning-based optimization: a novel method for constrained
1193 mechanical design optimization problems, *Comput. Aided Des.*, 43(3), pp. 303–315, 2011.
- 1194 40. Solari, G.: *Wind science and engineering*. Springer, Switzerland, 2019.
- 1195 41. Solari, G.: Emerging issues and new frameworks for wind loading on structures in mixed climates. *Wind Struct.* 19,
1196 295-320, 2014.

1197 42. Solari, G., Burlando, M., De Gaetano, P., Repetto, M., P.: Characteristics of thunderstorms relevant to the wind
1198 loading of structures. *Wind Struct.* 20, 763-791, 2015.

1199 43. Solari, G., Burlando, M., Repetto, M., P.: Detection, simulation, modelling and loading of thunderstorm outflows to
1200 design wind-safer and cost-efficient structures. *J. Wind Eng. Ind. Aerodyn.*, 200, 2020.

1201 44. Vicroy, D.D., 1991. A simple, analytical, axisymmetric microburst model for downdraft estimation. NASA Technical
1202 Memorandum 104053.

1203 45. Vicroy, D.D., 1992. Assessment of microburst models for downdraft estimation. *J. Aircraft* 29, 1043–1048.

1204 46. Ward, J., H., Jr.: Hierarchical Grouping to Optimize an Objective Function. *Journal of the American Statistical*
1205 *Association*, Volume 58, Issue 301, 236-244, 1963.

1206 47. Weisman, M. L.: Bow echoes: A tribute to T.T. Fujita. *Bulletin of the American Meteorological Society*, 82(1), 97-
1207 116, 2001.

1208 48. Xhelaj, A., Burlando, M., Solari, G.: A general-purpose analytical model for reconstructing the thunderstorm
1209 outflows of travelling downbursts immersed in ABL flows. *J Wind Eng. Ind. Aerodyn.* 207 104373, 2020.

1210 49. Xhelaj, A., Burlando, M.: Application of metaheuristic optimization algorithms to evaluate the geometric and
1211 kinematic parameters of downbursts. *Advances in Engineering Software*. Volume 173, November 2022, 103203.,
1212 2022.

1213

1214

1215